Monthly Notices of the ROYAL ASTRONOMICAL SOCIETY

MNRAS **534,** 783–799 (2024) https://doi.org/10.1093/mnras/stae2137
Advance Access publication 2024 September 13

The PIPER survey. II. The globular cluster systems of low surface brightness galaxies in the Perseus cluster

Steven R. Janssens [1]★ Duncan A. Forbes,[1]★ Aaron J. Romanowsky [2,3,4] Jonah Gannon [1] Joel Pfeffer [1] Warrick J. Couch,[1] Jean P. Brodie,[1] William E. Harris,[5] Patrick R. Durrell[6] and Kenji Bekki[7]

[1]*Centre for Astrophysics and Supercomputing, Swinburne University, Hawthorn VIC 3122, Australia*
[2]*Department of Physics & Astronomy, San José State University, One Washington Square, San Jose, CA 95192, USA*
[3]*Department of Astronomy & Astrophysics, University of California, Santa Cruz, CA 95064, USA*
[4]*University of California Observatories, 1156 High Street, Santa Cruz, CA 95064, USA*
[5]*Department of Physics & Astronomy, McMaster University, 1280 Main Street West, Hamilton, L8S 4M1, Canada*
[6]*Department of Physics, Astronomy, Geology and Environmental Sciences, Youngstown State University, Youngstown OH 44555, USA*
[7]*ICRAR, The University of Western Australia, 35 Stirling Hwy, Crawley WA 6009, Australia*

Accepted 2024 September 9. Received 2024 September 8; in original form 2024 January 16

ABSTRACT

We present *Hubble Space Telescope* ACS/WFC and WFC3/UVIS imaging for a sample of 50 low-surface brightness (LSB) galaxies in the $\sim 10^{15}$ $M_\odot$ Perseus cluster, which were originally identified in ground-based imaging. We measure the structural properties of these galaxies and estimate the total number of globular clusters (GCs) they host. Around half of our sample galaxies meet the strict definition of an ultra-diffuse galaxy (UDG), while the others are UDG-like but are either somewhat more compact or slightly brighter. A small number of galaxies reveal systems with many tens of GCs, rivalling some of the richest GC systems known around UDGs in the Coma cluster. We find the sizes of rich GC systems, in terms of their half-number radii, extending to ∼1.2 times the half-light radii of their host galaxy on average. The mean colours of the GC systems are the same, within the uncertainties, as those of their host galaxy stars. This suggests that GCs and galaxy field stars may have formed at the same epoch from the same enriched gas. It may also indicate a significant contribution from disrupted GCs to the stellar component of the host galaxy as might be expected in the 'failed galaxy' formation scenario for UDGs.

Key words: galaxies: dwarf – galaxies: formation – galaxies: star clusters: general.

1 INTRODUCTION

Ultra-diffuse galaxies (UDGs) are a class of extended low-surface brightness (LSB) galaxies. Their abundance in galaxy clusters was discovered with the Dragonfly Telephoto Array where a large population of galaxies with effective radii $R_e \gtrsim 1.5$ kpc and central surface brightnesses $\mu_{0,g} \gtrsim 24$ mag arcsec^{-2} were identified in the Coma cluster (van Dokkum et al. 2015).

High resolution imaging of Coma cluster UDGs with the *Hubble Space Telescope* (*HST*) revealed some to have remarkably rich globular cluster (GC) systems for galaxies with stellar masses of around 10^8 $M_\odot$ (van Dokkum et al. 2017; Amorisco et al. 2018; Lim et al. 2018). This was further reinforced by Forbes et al. (2020) who combined the GC counts from these three studies. While some Coma UDGs were consistent with hosting no GCs, others hosted up to a hundred GCs. For example, Dragonfly (DF) 44 was estimated by van Dokkum et al. (2017) to have 76 ± 18 GCs. However, also using *HST* imaging, Saifollahi et al. (2022) examined six Coma UDGs and found much lower counts than van Dokkum et al. (2017) or Lim et al. (2018). For DF44, Saifollahi et al. (2022) suggested a total GC system of 20^{+6}_{-5}. Forbes & Gannon (2024) have shown that the lower GC counts of Saifollahi et al. (2022) are driven by their measured GC system size (half-number radius) relative to the galaxy half-light radius. While Forbes & Gannon (2024) favoured the numbers found by van Dokkum et al. (2017) and Lim et al. (2018), without spectra of GC candidates, it is unlikely this matter will be fully settled in the near future.

The GC systems of UDGs in a number of other clusters have also been studied. These include Fornax (Prole et al. 2019), Virgo (Lim et al. 2020b), and Hydra I (La Marca et al. 2022), but few, if any, UDGs possess the rich GC systems found in the Coma cluster. This, along with the claims of Saifollahi et al. (2022), have led some to question the reliability of the rich GC systems in Coma UDGs. Another possibility is that only the most massive clusters like Coma host a population of UDGs with rich GC systems. Clearly, an equivalent *HST* study of a cluster with a total mass similar to Coma ($0.5 < M_{200} < 1.25 \times 10^{15}$ $M_\odot$; Ho et al. 2022) is required.

As well as determining the ratio of GC system to galaxy size, another important measurement is the mean colour of the GC system and how it compares with the host galaxy light. If galaxy stars formed independently of the GCs and over a longer period,

★ E-mail: steven.janssens@utoronto.ca (SRJ); dforbes@swin.edu.au (DAF)

then we might expect the galaxy to be on average redder than the GCs. However, a similar colour would suggest a similar age and metallicity for GCs and galaxy stars, indicating that they may have formed from the same enriched gas at the same epoch. Such stellar populations might be expected in the 'failed galaxy' formation scenario whereby GCs form and, by some mechanism, the host galaxy is quenched at early times (Danieli et al. 2022; Forbes & Gannon 2024). Disruption of GCs over time will contribute field stars to the host galaxy. If the stars from disrupted GCs dominate the luminosity of the galaxy, then similar mean colours in the remaining GCs and the galaxy stars would be measured. In a recent detailed analysis of the colours of GCs in two UDGs (DF2 and DF4 in the NGC 1052 group) by van Dokkum et al. (2022), they found that in both cases, the GCs are slightly redder on average than their host galaxy.

We present multiband *HST* imaging of the Perseus cluster obtained as part of the Program for Imaging of the PERseus cluster of galaxies (PIPER) survey (Harris et al. 2020, hereafter, Paper I). The large scale structure of GCs and their spatial associations on the sky have been previously examined by Paper I and Li et al. (2022). Here, we measure galaxy properties using *HST* for a sample of 50 LSB galaxies originally identified in ground-based imaging. Measured properties include their magnitudes, mean colours, half-light radii, and ellipticities. We also identify their GC candidates and, after correcting for incompleteness and contamination, estimate their total GC numbers. We measure the half-number radii and mean colours of the GC systems, and compare them to the host galaxy. We follow Paper I and adopt a distance $d = 75$ Mpc to the Perseus cluster, which corresponds to a distance modulus $\mu = 34.38$. Perseus has a virial radius $R_{200} = 1.79 \pm 0.04$ Mpc and a total mass $M_{200} = 6.65^{+0.43}_{-0.46} \times 10^{14}$ $M_\odot$ based on X-ray observations of the intracluster medium (Simionescu et al. 2011). Aguerri et al. (2020) measured a larger more massive cluster with $R_{200} = 2.2$ Mpc and $M_{200} = 1.2 \times 10^{15}$ $M_\odot$ from spectroscopic measurements of 403 galaxies in Perseus. Thus, the Perseus cluster has a mass similar to that of the Coma cluster (whose UDG population has been well studied). All photometry is in the VEGAmag system. Galactic extinction is quite high in the direction of the Perseus cluster with up to $A_V \sim 0.5$. This means the galaxies and GCs are effectively as faint as in the Coma cluster, but they are still slightly better resolved. Here, we apply corrections from the Schlafly & Finkbeiner (2011) extinction maps to all colours and magnitudes..[1]

2 DATA AND METHODS

2.1 *HST* observations

The programme for Imaging of the PERseus cluster of galaxies (PIPER) used ACS/WFC and WFC3/UVIS aboard *HST* in parallel to observe ten pairs of fields outside of the Perseus cluster core and five focused on NGC 1275 and other giant cluster galaxies in the core (see fig. 1 of Paper I for the arrangement of the fields). The field pairs, or 'visits', were chosen to contain 50 LSB galaxies. They were selected from the catalogue of Perseus LSB galaxies by Wittmann et al. (2017) (33 targets, designated W) and supplemented by additional LSB targets found through visual inspection of archival G'- and R'-band CFHT/MegaCam imaging[2] (17 targets, designated R), whose UDG-like nature was confirmed using GALFIT (Peng et al. 2002). The target selection prioritized the largest UDG-like galaxies ($R_e \gtrsim 2$ kpc) while also including as many LSB galaxies as possible in each visit. The five core fields cover the inner ∼230 kpc (∼3 arcmin) around NGC 1275. The outer fields range from a minimum distance of ∼240 kpc (∼11 arcmin) from NGC 1275 out to a maximum of ∼780 kpc (∼36 arcmin), with a mean distance of ∼475 kpc (∼22 arcmin), though the sampling is fairly uniform and there is a strong bias to the West side of the cluster. One target, W27, turned out to not exist at the given coordinates in the Wittmann et al. (2017) catalogue.

Each visit was observed for two orbits. For ACS, one orbit used the F814W filter and the other F475W. For WFC3, F814W, and F475X were the two filters used. The calibrated, flat fielded and charge transfer efficiency (CTE) corrected individual exposures (`flc` files) were obtained from MAST. For each exposure, we ensured that either a *GAIA* DR2 or DR3 *a posteriori* WCS solution contained in an extension headerlet was applied. These were combined using AstroDrizzle to a final pixel scale of 0.03 arcsec, and were weighted with an inverse-variance weight map. Exposure time maps were obtained by running AstroDrizzle a second time, and weighting by exposure time, with the other products being discarded. We were notified of guiding issues potentially affecting the visits to PERSEUS-UDG02, PERSEUS-UDG06, and NGC1275-F1 (see table 1 of Paper I for details of all the visits). However, only a single WFC3 F475X exposure for the PERSEUS-UDG02 visit exhibited streaks indicative of a loss of guiding. The affected `flc` file was removed before combining with AstroDrizzle. With only two remaining exposures, this image is more contaminated by cosmic rays compared to the others.

2.2 Photometry

SExtractor (Bertin & Arnouts 1996) was run in dual-image mode on each image pair (F475W/F814W for ACS, F475X/F814W for WFC3) using the F814W image as the detection image. Magnitudes were measured in 5 pixel diameter apertures. Since the purpose of this catalogue is to detect unresolved or marginally resolved GCs and not galaxies, a very small background cell size of `BACK_SIZE` = 24 pixels was used. This both aids in the detection of GCs by subtracting off large scale structure, including the stellar bodies of galaxies, as well as provides a more accurate background measurement. As a final aid in ensuring our GC detection is complete around our target galaxies, we subtracted off the best-fitting Imfit (Erwin 2015) model (described in Section 2.6) before running SExtractor. All magnitudes were placed on the VEGAmag system[3]. ACStools (Lim et al. 2020a) was used to retrieve the VEGAmag zeropoints for the ACS images, and stsynphot (STScI Development Team 2020) was used to calculate them for the WFC3 images. Galactic extinction values (Schlafly & Finkbeiner 2011) vary by several tenths of a magnitude from field to field. Here, we used the extinction value for the centre of each field and applied that to all sources within.

[1] Using the online calculator at https://ned.ipac.caltech.edu/forms/calculator.html. The maps have a resolution of a few arcmin, while deep imaging of Perseus from Subaru Hyper Suprime-Cam (Gannon et al. 2022) shows strong cirrus variations on scales of a few arcsec. This effect will introduce additional scatter in our photometric measurements (particularly for galaxies R16, R23, R79, W1, W5, W8, W22, W28, W29).

[2] The MegaPipe (Gwyn 2008) processed images are available from the Canadian Astronomy Data Centre with `observationID-MegaPipe.075.263`.

[3] VEGAmag was chosen over AB as the Paper IF475X_{WFC3} to F475W_{ACS} transformation is defined in the Vega system.

Aperture corrections were then applied. For the ACS images, we first corrected from a 5 pixel diameter aperture to a 1 arcsec diameter aperture by computing the encircled energy using a DAOPHOT model point spread function (PSF; see Section 2.3) for each image. We then corrected from the 1 arcsec diameter aperture to infinity using table 5 in Sirianni et al. (2005).[4] We performed the same procedure for the WFC3/UVIS magnitudes, but instead used the UVIS2 encircled energy fractions[5] to correct from a 1 arcsec diameter aperture to infinity. For ACS, the total 5 pixel to infinity diameter aperture correction values range from 0.79 to 0.94 mag for F814W and 0.67–0.88 mag for F475W, with the range due to the PSF variation between *HST* visits. For WFC3, the total aperture correction values are 0.67–0.80 mag for F814W and 0.59–0.87 mag for F475X.

We placed all photometry on the ACS system. Deustua & Mack (2018) found $F814W_{WFC3} \simeq F814W_{ACS}$. For the WFC3 fields, the blue filter is F475X. Following Paper I, we transformed F475X to $F475W_{ACS}$ using

$$F475W_{ACS} = F475X_{WFC3} + (0.16 \pm 0.02)(F475X - F814W)_{WFC3}. \quad (1)$$

There is a small region of overlap between the ACS and WFC3 imaging on the outskirts of NGC 1275 yielding 133 point sources with both ACS and WFC3 photometry, the vast majority of which have colours and magnitudes consistent with GCs. The distribution of WFC3 derived $(F475W - F814W)_{ACS}$ colours agrees well with the native ACS colours for these objects; the mean colour difference is 0.00 with a standard deviation of 0.27.

2.3 Artificial star tests and completeness limits

DAOPHOT (Stetson 1987) was used to construct a model PSF for each *HST* ACS and WFC3 image in each filter. The exposure times in the headers were used to convert the images from units of electrons per second to electrons, which is necessary for DAOPHOT to understand the noise. We followed the standard DAOPHOT procedure of running the `FIND`, `PHOT`, and `PICK` commands to select suitable PSF stars in each image. These were run without any user intervention. We then culled the list of PSF stars created by `PICK` by cross matching it to a list of suitable bright stars selected *a priori* from the SExtractor catalog. Suitable PSF stars have `FLAGS` = 0 (i.e. no photometry issues with this object), 18 < `MAG_AUTO` < 23.5, 1.25 pixels < `FLUX_RADIUS` < 3.25 pixels, no bad or empty pixels within the DAOPHOT fitting radius ($r = 10$ pixels) and no neighbours within the DAOPHOT PSF radius ($r = 51$ pixels). The number of PSF stars varies from 25 stars in the NGC1275-F5 WFC3 F475X image to over 200 in the NGC1275-F1 ACS F814W image. We adopt DAOPHOT defaults in defining the PSF model, namely a Gaussian analytic profile along with an empirical lookup table of corrections. Given the small expected variation of the PSF across a given field, no spatial variation of the PSF was applied. We then used the `ADDSTAR` routine in `DAOPHOT` to create an image of the PSF model to use for all subsequent tasks.

Artificial star tests were then performed by scaling the PSF images to the desired total magnitude and adding them to our images. We selected 5000 random positions in each F814W and F475W/F475X image pair. The SExtractor segmentation maps were used to ensure a selected location was empty. Note that, due to the small SExtractor background cell size used, most of the pixels belonging to UDGs and other galaxies are empty in the segmentation maps and thus are valid regions to inject artificial stars. The F814W total magnitudes of the artificial stars were drawn uniformly between 22.5 < F814W < 29.5. An F475W–F814W colour was then drawn from a skewnormal distribution with mean $\mu = 0.7$, standard deviation $\sigma = 1.6$ and skewness parameter $\alpha = 10$ in order to roughly match the observed colour range and distribution, with most sources (and GCs) having F475W–F814W $\lesssim 2$ (Paper I). When injecting sources into a WFC3 image, the F475W magnitude was transformed to F475X by inverting equation (1). Finally, Galactic extinction was added back on to the injected magnitudes.

The injected images were then processed in an identical manner to the real images. The artificial sources were recovered by matching the nearest detection within a maximum distance of 3 pixels (0.09 arcsec) from the expected position, with no other restrictions on a match. Fig. A1 shows the recovered fraction of artificial stars in F814W with bins of 0.25 magnitudes. The completeness curves were fitted using

$$f(m) = \frac{1}{1 + e^{\alpha(m - m_{50})}}, \quad (2)$$

where m_{50} is the magnitude at which the recovered fraction has dropped to 50 per cent and α controls how steeply the completeness drops off (Harris et al. 2016). The observed depths between visits for each camera are very similar, with the observed variation simply reflecting the extinction variations in this part of the sky. The dotted lines show the completeness level at the expected GCLF turnover magnitude $m_{TO,F814W} = 26.3$, corresponding to $M_{TO,I} = -8.1$ (Miller & Lotz 2007) at a distance of 75 Mpc. The data are between 71 per cent and 97 per cent complete at the turnover magnitude in every field, and at least 80 per cent complete in all UDG fields, with an average completeness at $m_{TO,F814W}$ of 87 per cent.

2.4 Point source selection

Fig. 1 shows our selection of point sources based on their concentration C_{5-12}, the difference in F814W magnitude measured in 5 and 12 pixel diameter apertures. Sources from all fields are shown. In black are all our artificial stars, and in gold are a representative subset of real sources from the images. Since the PSF is slightly different between the two cameras, a slightly different selection has to be made for each camera. The dashed vertical red curves are our adopted magnitude dependent point source selection that encompasses most of our artificial stars. The selection broadens from a minimum of ±0.13 from the mean concentration value for ACS (±0.11 for WFC3) to a maximum of ±0.40 for both cameras. These extremes were estimated from the brightest and faintest artificial stars, with the value at the faint end chosen as a compromise between encompassing as many artificial stars as possible and minimizing the number of contaminants. Between these extremes, we fitted the observed standard deviation of C_{5-12} of artificial stars as a function of magnitude with an exponential function and selected all detections within $\pm 2\sigma$.

To check that GCs at 75 Mpc would pass these concentration cuts, we used GALFIT (Peng et al. 2002) to create King (1962) profiles convolved with our PSFs and measured the resulting C_{5-12}. We simulated objects with core radii between 0.5 and 10 pc and $1.5 < \log(r_t/r_c) < 2.5$, where r_t and r_c are the tidal and core radii, respectively, thus spanning GCs to ultra-compact dwarfs (UCDs;

[4]The difference between the Sirianni et al. (2005) and the more recent Bohlin (2016) ACS aperture corrections are negligible, at 0.006 mag and 0.01 mag for F475W and F814W, respectively, and have no impact on the results.
[5]https://www.stsci.edu/hst/instrumentation/wfc3/data-analysis/photometric-calibration/uvis-encircled-energy

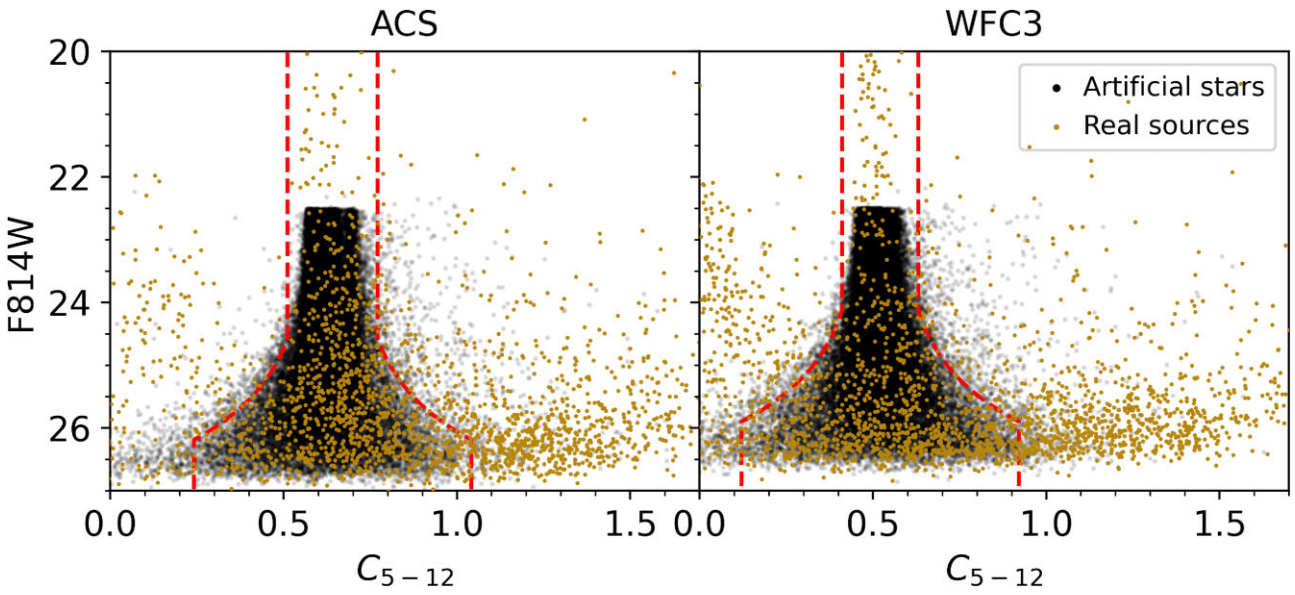

Figure 1. Concentration based selection of point sources. C_{5-12} is the difference in F814W magnitude between 5 and 12 pixel diameter apertures. Since the PSF differs slightly between the ACS/WFC and WFC3/UVIS cameras, a selection for each is made based on the observed locus of artificial stars. The black points are our artificial stars and the gold points show a representative subset of our real sources. The dashed red curves are our point source selection boundaries, which encompass the bulk of our artificial stars. See the text for details.

Evstigneeva et al. 2008). Half-light radii r_h were measured on a separate high-resolution model without PSF convolution. Objects with $r_h \lesssim 5$ pc pass our point source cuts, which matches the expected resolution limit of *HST* at 75 Mpc (we refer the reader to section 4.1 of Paper I for a discussion on the size distribution of intracluster GC candidates in a handful of the outer fields). A clean point source selection with fewer background galaxy contaminants comes at the cost of possibly missing a fraction of GCs with larger radii that are partially resolved. However, we believe this fraction to be low as inspection of sources around our sample galaxies reveals only a handful of compact sources that fail this point source cut but have the magnitudes and colours of GCs (see Sectyion 2.5).

2.5 Globular cluster selection

At a distance of 75 Mpc, GCs in the Perseus cluster are essentially point sources when imaged by the *HST*. From point sources, GCs were selected on the basis of magnitude and colour. Fig. 2 shows the colour–magnitude diagram of all point sources in the F475W and F814W filters. WFC3 sources have been transformed to the ACS filter system and are plotted in gold. The dashed red box shows our GC selection which comprises all point sources $21.5 < \mathrm{F814W} < 26.3$, and within the colour range $0.8 < \mathrm{F475W} - \mathrm{F814W} < 2.4$. The faint limit corresponds to the predicted GCLF turnover magnitude. The bright magnitude cutoff corresponds to a generous stellar mass for a GC of $\sim 10^7$ $M_\odot$ and so would accommodate objects classified as UCDs. However, examination of Fig. 2 shows there are very few sources brighter than F814W $\sim$ 22 – though such UCDs may have failed the concentration cuts. The red error bars on the left-hand side show characteristic colour errors from the artificial star tests in bins of 0.5 mag, restricted to artificial stars with a colour inside the GC selection box. The red and blue ticks along the bottom show the predicted colours for a large possible range of properties spanned by GCs using FSPS (Conroy, Gunn & White 2009; Conroy & Gunn 2010). The blue tick has an age of 5 Gyr and is metal poor with $[\mathrm{Fe/H}] = -2.2$. The red tick is 13 Gyr old and is metal rich with $[\mathrm{Fe/H}] = 0.6$. While it is unlikely an individual GC would possess these properties, this exercise is merely to ascertain the colour range in which we expect GCs to fall. Our GC colour selection was expanded beyond this range to account for the large photometric scatter at faint magnitudes.

2.6 Galaxy fitting

We used IMFIT[6] (Erwin 2015) to fit a single component Sérsic model plus a sky pedestal to the F814W and F475W/F475X image of each of the 50 known UDGs targeted as part of this program. IMFIT was run on 150 arcsec × 150 arcsec cutouts centred on each galaxy in MCMC mode. Since the cutouts are in units of electrons s^{-1} and were sky subtracted by ASTRODRIZZLE, the total exposure time and original sky value (computed from the `MDRIZSKY` values in the `flc` headers) were passed to `imfit-mcmc`. Other sources in the cutouts were excluded by first masking all pixels belonging to other objects in the SEXTRACTOR segmentation map. Note that, the mask includes any GCs or nuclei, preventing them – particularly central nuclei – from impacting the fit. We then expanded the masks around sources by masking all pixels within a Kron ellipse of a source with semi-major axis equal to 3 × `A_IMAGE` × `KRON_RADIUS`. The semi-major axis of the mask ellipse was not permitted to be less than 20 pixels (0.6 arcsec). Note that, the mask expansion was not done for sources within 10 arcsec of the centre of the galaxy. Bad and empty pixels were masked by masking pixels with 0 values in the exposure time maps. The masks were then manually tweaked to mask scattered light and ghosts from bright stars, or inadequate automatic masking of neighbours. As the galaxies are all brighter in the red, the position of the F475W/F475X fit was fixed to the fitted F814W position. We also adopt the F814W values when reporting results.

The best-fitting parameters are the 50 per cent percentile from the posterior distributions, with 16 per cent and 84 per cent uncertainties.

[6] https://www.mpe.mpg.de/~erwin/code/imfit/

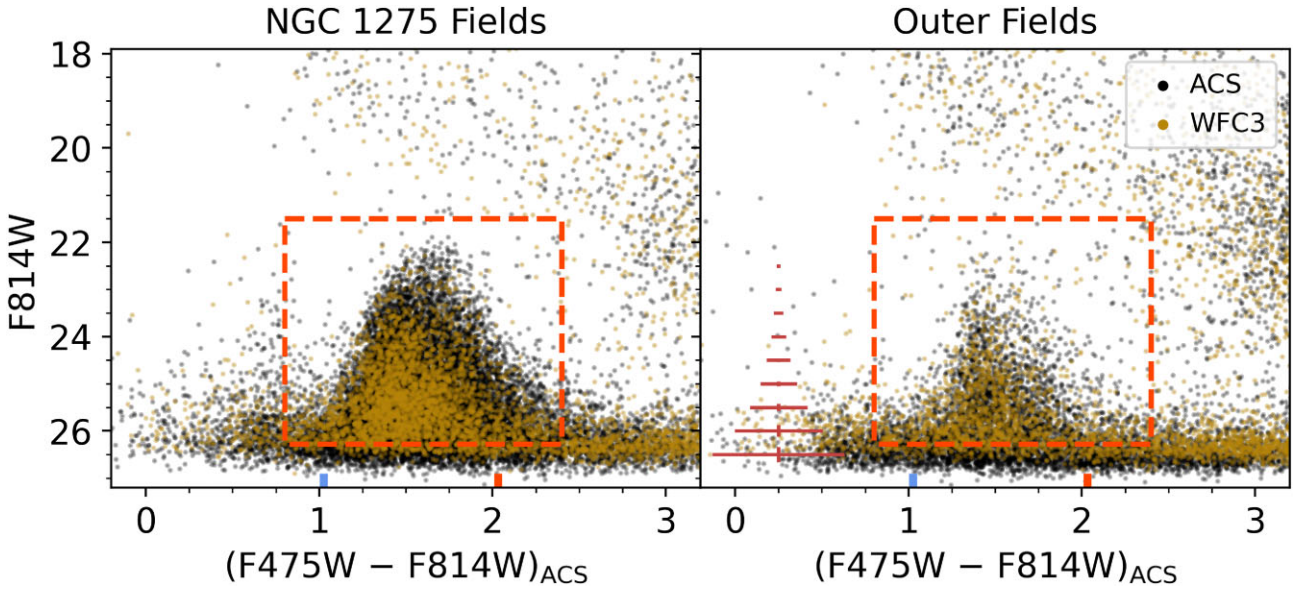

Figure 2. Combined ACS and WFC3 F475W/F814W colour–magnitude diagrams of point sources showing our selection of GCs. Sources from the cluster core NGC 1275 fields are shown in the left panel, while the right panel shows sources from the outer fields. WFC3 photometry (gold points) has been transformed to the ACS system (see the main text for details). The dashed red boxes show our GC selection of $0.8 <$ F475W–F814W < 2.4 and $21.5 <$ F814W < 26.3, the faint end of which is the predicted turnover magnitude of the GCLF. The blue and red ticks along the bottom show the predicted colours of SSPs with the most extreme possible GC properties. The blue tick is a 5 Gyr old GC with [Fe/H] $= -2.2$. The red tick is 13 Gyr old and has [Fe/H] $= 0.6$. The red error bars on the left are characteristic errors from the artificial star tests.

Model images were created by passing the best-fitting parameters to IMFIT's `makeimage` executable. The model image was then subtracted off to create a residual image. Fig. 3 shows the F814W IMFIT results for 5 UDGs. In each row, from left to right, is shown the original F814W image, the residual after subtraction of the best-fitting model, the model itself, the original image after masking bad pixels and pixels belonging to other sources and finally the masked residual image. Each cutout is 13 kpc on a side (∼36 arcsec) at the adopted distance of 75 Mpc to the cluster. The colour is then measured on the model images using a fixed circular aperture 1 kpc in diameter, with F475X transformed to F475W using equation (1). Such an aperture provides a reliable colour, albeit for the more central regions. The colour uncertainties are estimated from the posterior distribution of total magnitudes, computed using equation 2 in Graham & Driver (2005).

3 RESULTS AND DISCUSSION

3.1 Galaxy structural properties

Table 1 lists the structural properties of the 50 sample galaxies, including coordinates, total magnitudes, surface brightnesses (mean and central), colours within 1 kpc, and Sérsic profile parameters (i.e. half-light radii, Sérsic index and axis ratios b/a). All parameters were measured in F814W, with adopted values being the 50 per cent percentiles from the IMFIT posterior distributions, with 16 per cent and 84 per cent percentile uncertainties. The MCMC mode of IMFIT was chosen as it provides slightly larger and more realistic uncertainties than χ^2 minimization. While the uncertainties may still be underestimated, we note that the more important quantity of interest is the ratio of the size of the GC system ($R_{\rm GC}$) to the galaxy, for which the uncertainty will be dominated by $R_{\rm GC}$ (see Section 3.3).

Five galaxies (R79, W14, W29, W36, and W80) could not be modelled successfully with IMFIT. This was due to bright stars or strong artefacts that resulted in too little galaxy light after masking, or the galaxy was simply too faint to model. An additional four galaxies were not fitted in the F475W filter. Thus, structural *and* colour information is only available for 41 of the 50 galaxies in the sample.

van Dokkum et al. (2015) originally defined UDGs as those with $R_{\rm e} \gtrsim 1.5$ kpc and $\mu_{0,g} \gtrsim 24$ AB mag arcsec^{-2}, where $R_{\rm e}$ is the half-light radius measured along the major axis and $\mu_{g,0}$ is the central surface brightness in the g-band in AB magnitudes. In Fig. 4, we plot the F814W half-light radius along the major-axis and the central surface brightness in F475W, which is similar to SDSS g band. The F475W central surface brightness is estimated from the F814W central surface brightness and the model colour with $\mu_{0,\rm F475W} = \mu_{0,\rm F814W} +$ (F475W–F814W). The dashed line shows the UDG selection criteria. Here, we are using Vega magnitudes instead of AB, which amounts to a difference of $\Delta{\rm F475W}_{\rm AB-VEGA} = -0.1$. So in Vega magnitudes, the bright surface brightness limit is $\mu_{\rm F475W,0} \approx 24.1$ mag arcsec^{-2}. Of the 50 LSB galaxies listed in Table 1, we plot the 41 that have *both* measured structural parameters and a colour. Black circles denote the 23 LSB galaxies which strictly pass the UDG criteria, whereas blue squares include 2 UDG-like objects (W4 and R27) that are somewhat brighter and 16 that are more compact than UDGs. These symbol definitions will be preserved in subsequent figures. Galaxies that do not meet the strict UDG definition (i.e. those with $R_{\rm e} < 1.5$ kpc or $\mu_{0,\rm F475W} < 24.1$ mag arcsec^{-2}, or missing the information to make the determination) are listed at the end of the table.

Since the UDG definition is rather arbitrary, it is perhaps no surprise that it does not identify a distinct population of galaxies but rather a continuous distribution in both size and surface brightness. Some of the UDG-like galaxies, outside of the UDG selection box, in Fig. 4 could be referred to as NUDGEs (Forbes & Gannon

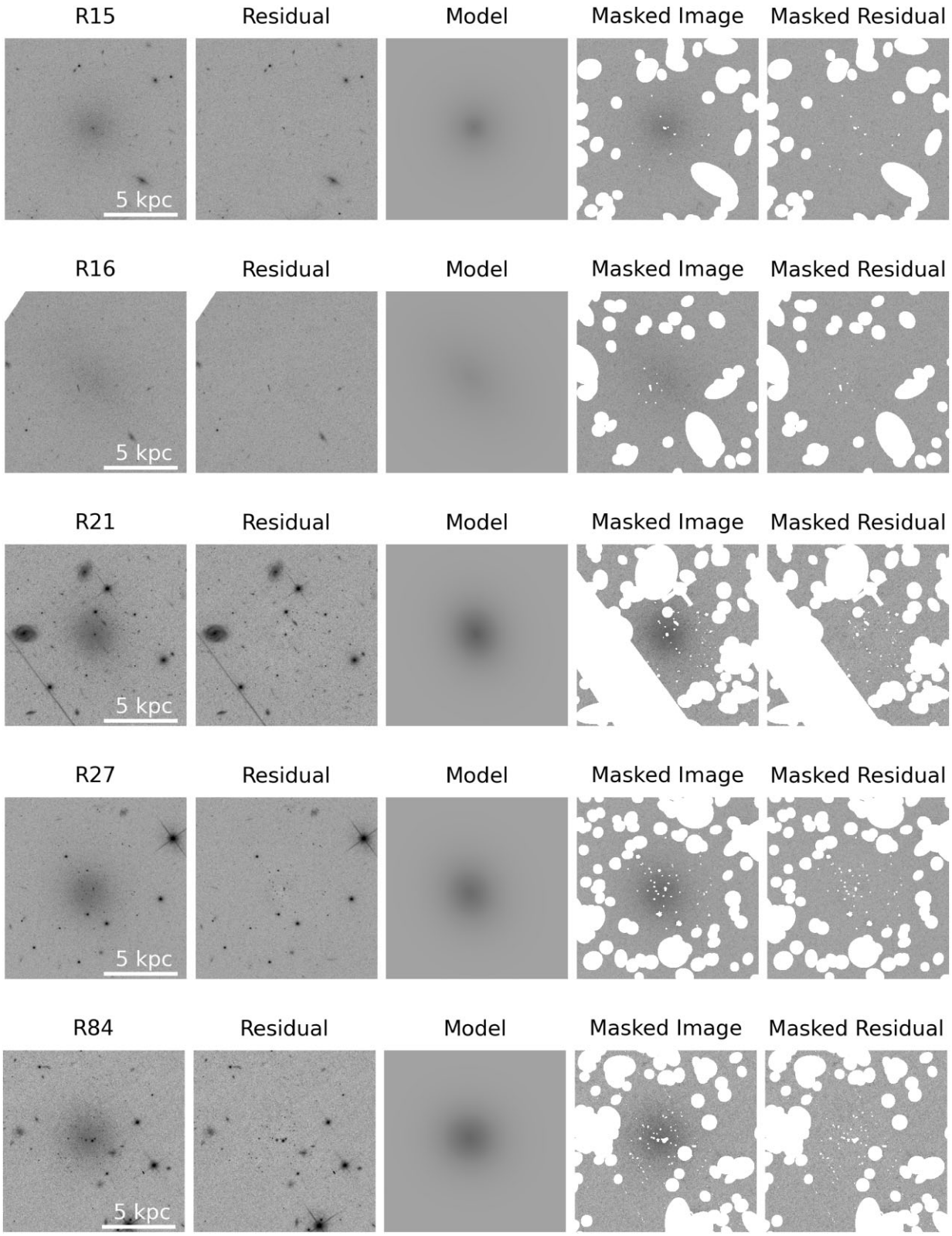

Figure 3. IMFIT results for five example galaxies (among the most luminous in the sample): R15, R16, R21, R27, and R84. The cutouts are 13 kpc on a side (∼36 arcsec) with North oriented up and East to the left. For each galaxy, from left to right, is shown the *HST*/ACS F814W image, the residual image after model subtraction, the IMFIT model image, the image with mask applied, and the residual image with mask applied. The mask includes any central nuclei (e.g. R21).

Table 1. Structural properties of PIPER LSBs. $M_{\rm F814W}$ is the F814W absolute magnitude, adopting $d = 75$ Mpc. $\langle\mu\rangle_{\rm e,F814W}$ and $\mu_{0,\rm F814W}$ are the mean surface brightness within $R_{\rm e}$ and central surface brightness, respectively. The F475W–F814W colour is measured inside a 1 kpc diameter aperture on the models. $R_{\rm e}$ is the model effective radius measured along the major-axis, n is the Sérsic index and b/a is the axis ratio (with these parameters measured on the F814W images). LSB galaxies that meet the UDG definition are listed at the top, followed by those that are UDG-like but either more compact with $R_{\rm e} < 1.5$ kpc, too bright in F475W surface brightness, or missing the information needed to make this determination. Galaxies whose IDs are marked with † reside in the NGC 1275 core fields (R33, W74, and W87).

ID	α (J2000.0)	δ (J2000.0)	$M_{\rm F814W}$ (mag)	$\langle\mu\rangle_{\rm e,F814W}$ (mag/□″)	$\mu_{0,\rm F814W}$ (mag/□″)	F475W − F814W (mag)	$R_{\rm e}$ (kpc)	n	b/a
R5	03:17:34.6	41:45:21.6	$-15.94^{+0.12}_{-0.12}$	$24.56^{+0.05}_{-0.05}$	$23.79^{+0.09}_{-0.09}$	$1.59^{+0.35}_{-0.36}$	$2.72^{+0.07}_{-0.06}$	$0.78^{+0.03}_{-0.03}$	$0.80^{+0.01}_{-0.01}$
R6	03:16:58.9	41:42:10.1	$-15.91^{+0.07}_{-0.07}$	$23.76^{+0.03}_{-0.03}$	$23.10^{+0.05}_{-0.05}$	$1.57^{+0.19}_{-0.19}$	$1.78^{+0.02}_{-0.02}$	$0.71^{+0.02}_{-0.02}$	$0.87^{+0.01}_{-0.01}$
R14	03:17:06.1	41:13:03.2	$-14.45^{+0.20}_{-0.20}$	$24.76^{+0.09}_{-0.08}$	$24.23^{+0.14}_{-0.14}$	$1.34^{+0.43}_{-0.42}$	$1.54^{+0.05}_{-0.05}$	$0.62^{+0.04}_{-0.04}$	$0.76^{+0.03}_{-0.03}$
R15	03:17:03.8	41:14:55.0	$-16.63^{+0.07}_{-0.07}$	$23.73^{+0.03}_{-0.03}$	$22.67^{+0.06}_{-0.06}$	$1.55^{+0.18}_{-0.18}$	$2.31^{+0.03}_{-0.03}$	$0.97^{+0.02}_{-0.02}$	$0.98^{+0.01}_{-0.01}$
R16	03:18:36.5	41:11:32.1	$-17.23^{+0.09}_{-0.09}$	$24.26^{+0.04}_{-0.04}$	$23.31^{+0.07}_{-0.07}$	$1.68^{+0.32}_{-0.33}$	$4.57^{+0.10}_{-0.09}$	$0.90^{+0.02}_{-0.02}$	$0.71^{+0.01}_{-0.01}$
R20	03:20:24.6	41:43:28.6	$-14.95^{+0.16}_{-0.16}$	$24.51^{+0.07}_{-0.06}$	$24.01^{+0.11}_{-0.11}$	$1.02^{+0.37}_{-0.37}$	$1.72^{+0.05}_{-0.05}$	$0.60^{+0.03}_{-0.03}$	$0.77^{+0.02}_{-0.02}$
R21	03:20:29.5	41:44:51.0	$-16.46^{+0.07}_{-0.07}$	$23.61^{+0.03}_{-0.03}$	$22.54^{+0.06}_{-0.06}$	$1.63^{+0.25}_{-0.24}$	$2.16^{+0.03}_{-0.03}$	$0.97^{+0.02}_{-0.02}$	$0.85^{+0.01}_{-0.01}$
R23	03:19:51.5	41:54:35.6	$-16.44^{+0.09}_{-0.10}$	$24.06^{+0.04}_{-0.04}$	$23.33^{+0.07}_{-0.07}$	$1.70^{+0.22}_{-0.22}$	$2.58^{+0.05}_{-0.05}$	$0.76^{+0.02}_{-0.02}$	$0.89^{+0.01}_{-0.01}$
R25	03:18:26.3	41:41:52.2	$-15.52^{+0.14}_{-0.14}$	$24.75^{+0.06}_{-0.06}$	$24.19^{+0.11}_{-0.10}$	$1.11^{+0.26}_{-0.25}$	$2.69^{+0.06}_{-0.06}$	$0.65^{+0.03}_{-0.03}$	$0.66^{+0.02}_{-0.02}$
R33†	03:20:25.8	41:31:11.9	$-16.61^{+0.10}_{-0.10}$	$23.76^{+0.04}_{-0.04}$	$22.91^{+0.07}_{-0.07}$	$1.60^{+0.28}_{-0.27}$	$2.58^{+0.06}_{-0.05}$	$0.83^{+0.02}_{-0.02}$	$0.78^{+0.01}_{-0.01}$
R84	03:17:24.9	41:44:21.5	$-16.31^{+0.06}_{-0.06}$	$23.68^{+0.02}_{-0.02}$	$22.91^{+0.05}_{-0.04}$	$1.53^{+0.18}_{-0.18}$	$1.99^{+0.02}_{-0.02}$	$0.78^{+0.01}_{-0.01}$	$0.94^{+0.01}_{-0.01}$
W1	03:17:00.4	41:19:20.6	$-15.98^{+0.07}_{-0.07}$	$23.65^{+0.03}_{-0.03}$	$22.70^{+0.05}_{-0.05}$	$1.43^{+0.38}_{-0.38}$	$1.80^{+0.02}_{-0.02}$	$0.90^{+0.02}_{-0.02}$	$0.83^{+0.01}_{-0.01}$
W5	03:17:10.9	41:34:03.6	$-15.33^{+0.15}_{-0.15}$	$24.36^{+0.06}_{-0.06}$	$23.78^{+0.11}_{-0.11}$	$1.55^{+0.35}_{-0.35}$	$1.99^{+0.05}_{-0.05}$	$0.66^{+0.03}_{-0.03}$	$0.71^{+0.02}_{-0.02}$
W8	03:17:19.6	41:34:32.0	$-13.68^{+0.25}_{-0.25}$	$25.57^{+0.10}_{-0.10}$	$25.54^{+0.11}_{-0.13}$	$1.46^{+0.66}_{-0.67}$	$1.82^{+0.07}_{-0.07}$	$0.20^{+0.05}_{-0.04}$	$0.56^{+0.04}_{-0.04}$
W12	03:17:36.7	41:23:00.9	$-15.33^{+0.16}_{-0.16}$	$23.94^{+0.07}_{-0.07}$	$22.83^{+0.14}_{-0.15}$	$1.75^{+0.32}_{-0.30}$	$1.59^{+0.05}_{-0.04}$	$0.99^{+0.05}_{-0.04}$	$0.75^{+0.02}_{-0.02}$
W17	03:17:44.1	41:21:18.7	$-15.48^{+0.10}_{-0.10}$	$23.93^{+0.04}_{-0.04}$	$23.16^{+0.07}_{-0.07}$	$1.59^{+0.21}_{-0.21}$	$1.92^{+0.04}_{-0.04}$	$0.79^{+0.02}_{-0.02}$	$0.59^{+0.01}_{-0.01}$
W18	03:17:48.4	41:18:39.3	$-15.28^{+0.44}_{-0.43}$	$25.07^{+0.16}_{-0.15}$	$24.17^{+0.29}_{-0.28}$	$1.65^{+0.70}_{-0.70}$	$3.13^{+0.32}_{-0.29}$	$0.86^{+0.08}_{-0.08}$	$0.52^{+0.04}_{-0.03}$
W19	03:17:53.1	41:19:31.9	$-15.25^{+0.25}_{-0.25}$	$24.44^{+0.10}_{-0.10}$	$23.23^{+0.20}_{-0.20}$	$1.62^{+0.46}_{-0.46}$	$1.84^{+0.10}_{-0.09}$	$1.05^{+0.06}_{-0.06}$	$0.83^{+0.03}_{-0.03}$
W33	03:18:25.9	41:41:07.3	$-15.04^{+0.17}_{-0.18}$	$24.51^{+0.07}_{-0.07}$	$23.75^{+0.13}_{-0.13}$	$1.36^{+0.36}_{-0.34}$	$1.70^{+0.06}_{-0.05}$	$0.78^{+0.04}_{-0.04}$	$0.85^{+0.02}_{-0.02}$
W74†	03:19:22.0	41:27:23.0	$-15.71^{+0.10}_{-0.10}$	$23.93^{+0.04}_{-0.04}$	$23.34^{+0.07}_{-0.07}$	$1.64^{+0.30}_{-0.29}$	$1.70^{+0.03}_{-0.03}$	$0.67^{+0.02}_{-0.02}$	$0.93^{+0.02}_{-0.02}$
W79	03:19:39.2	41:12:05.6	$-15.47^{+0.13}_{-0.12}$	$24.36^{+0.05}_{-0.05}$	$23.42^{+0.10}_{-0.10}$	$1.46^{+0.26}_{-0.27}$	$2.22^{+0.05}_{-0.05}$	$0.89^{+0.03}_{-0.03}$	$0.65^{+0.02}_{-0.02}$
W88	03:19:59.1	41:18:32.4	$-17.42^{+0.13}_{-0.13}$	$24.30^{+0.04}_{-0.04}$	$23.01^{+0.08}_{-0.09}$	$1.49^{+0.31}_{-0.32}$	$5.44^{+0.17}_{-0.17}$	$1.10^{+0.02}_{-0.02}$	$0.61^{+0.01}_{-0.01}$
W89	03:20:00.1	41:17:05.4	$-14.81^{+0.15}_{-0.15}$	$24.70^{+0.06}_{-0.06}$	$24.17^{+0.11}_{-0.11}$	$1.20^{+0.44}_{-0.44}$	$1.83^{+0.05}_{-0.05}$	$0.63^{+0.03}_{-0.03}$	$0.71^{+0.02}_{-0.02}$
R27	03:19:43.6	41:42:46.8	$-17.12^{+0.04}_{-0.04}$	$23.05^{+0.02}_{-0.01}$	$22.23^{+0.03}_{-0.03}$	$1.61^{+0.09}_{-0.09}$	$2.23^{+0.02}_{-0.02}$	$0.82^{+0.01}_{-0.01}$	$0.88^{+0.01}_{-0.01}$
R60	03:19:36.2	41:57:26.2	$-15.60^{+0.08}_{-0.08}$	$23.67^{+0.03}_{-0.03}$	$22.96^{+0.06}_{-0.06}$	$1.46^{+0.33}_{-0.33}$	$1.42^{+0.02}_{-0.02}$	$0.75^{+0.02}_{-0.02}$	$0.95^{+0.01}_{-0.01}$
R79	03:18:21.2	41:46:15.3	–	–	–	–	–	–	–
R89	03:20:12.8	41:44:57.7	$-14.03^{+0.11}_{-0.11}$	$23.47^{+0.05}_{-0.04}$	$22.84^{+0.09}_{-0.09}$	$1.05^{+0.25}_{-0.24}$	$0.64^{+0.01}_{-0.01}$	$0.69^{+0.03}_{-0.03}$	$0.91^{+0.02}_{-0.02}$
R116	03:17:46.0	41:30:11.6	$-14.55^{+0.13}_{-0.13}$	$23.85^{+0.05}_{-0.05}$	$23.31^{+0.09}_{-0.09}$	$1.46^{+0.35}_{-0.37}$	$0.96^{+0.02}_{-0.02}$	$0.63^{+0.03}_{-0.03}$	$0.92^{+0.03}_{-0.02}$
R117	03:18:03.8	41:27:08.8	$-14.47^{+0.13}_{-0.13}$	$23.41^{+0.05}_{-0.05}$	$22.78^{+0.09}_{-0.10}$	$1.42^{+0.34}_{-0.35}$	$0.91^{+0.02}_{-0.02}$	$0.69^{+0.03}_{-0.03}$	$0.64^{+0.02}_{-0.02}$
W2	03:17:03.3	41:20:28.7	$-15.05^{+0.67}_{-0.74}$	$26.06^{+0.30}_{-0.28}$	$22.95^{+0.64}_{-0.64}$	–	$3.70^{+0.76}_{-0.51}$	$2.09^{+0.19}_{-0.18}$	$0.76^{+0.04}_{-0.04}$
W4	03:17:07.1	41:22:52.4	$-15.55^{+0.14}_{-0.14}$	$24.00^{+0.06}_{-0.06}$	$22.57^{+0.12}_{-0.12}$	$1.48^{+0.61}_{-0.63}$	$1.67^{+0.05}_{-0.05}$	$1.18^{+0.03}_{-0.03}$	$0.88^{+0.02}_{-0.02}$
W6	03:17:13.3	41:22:07.5	$-13.64^{+0.20}_{-0.21}$	$24.15^{+0.08}_{-0.08}$	$23.70^{+0.14}_{-0.14}$	$1.60^{+0.63}_{-0.61}$	$0.83^{+0.03}_{-0.03}$	$0.57^{+0.04}_{-0.04}$	$0.71^{+0.03}_{-0.03}$
W7	03:17:16.0	41:20:11.7	$-14.99^{+0.08}_{-0.08}$	$23.69^{+0.03}_{-0.03}$	$23.21^{+0.05}_{-0.05}$	$1.49^{+0.23}_{-0.24}$	$1.17^{+0.02}_{-0.02}$	$0.59^{+0.02}_{-0.02}$	$0.81^{+0.01}_{-0.01}$
W13	03:17:38.2	41:31:56.6	$-14.71^{+0.19}_{-0.19}$	$24.32^{+0.08}_{-0.08}$	$23.20^{+0.15}_{-0.16}$	$1.41^{+0.47}_{-0.46}$	$1.31^{+0.05}_{-0.04}$	$1.00^{+0.05}_{-0.05}$	$0.89^{+0.03}_{-0.03}$
W14	03:17:39.2	41:31:03.5	–	–	–	–	–	–	–
W16	03:17:41.8	41:24:02.0	$-13.91^{+0.23}_{-0.22}$	$24.70^{+0.09}_{-0.09}$	$24.27^{+0.15}_{-0.16}$	$1.59^{+0.52}_{-0.54}$	$1.31^{+0.05}_{-0.05}$	$0.56^{+0.05}_{-0.04}$	$0.61^{+0.03}_{-0.03}$
W22	03:18:05.4	41:27:42.1	$-15.42^{+0.12}_{-0.12}$	$24.45^{+0.05}_{-0.05}$	$23.81^{+0.10}_{-0.10}$	–	$2.11^{+0.05}_{-0.04}$	$0.70^{+0.03}_{-0.03}$	$0.74^{+0.02}_{-0.02}$
W25	03:18:15.5	41:28:35.3	$-14.80^{+0.13}_{-0.13}$	$23.77^{+0.06}_{-0.05}$	$23.16^{+0.10}_{-0.09}$	$1.51^{+0.36}_{-0.38}$	$1.31^{+0.03}_{-0.03}$	$0.68^{+0.03}_{-0.03}$	$0.59^{+0.02}_{-0.02}$
W28	03:18:21.7	41:45:27.5	$-13.30^{+0.21}_{-0.21}$	$24.13^{+0.08}_{-0.08}$	$23.87^{+0.13}_{-0.13}$	$1.36^{+0.71}_{-0.69}$	$0.63^{+0.02}_{-0.02}$	$0.42^{+0.04}_{-0.04}$	$0.89^{+0.04}_{-0.04}$
W29	03:18:23.3	41:45:00.6	–	–	–	–	–	–	–
W35	03:18:28.3	41:39:48.5	$-14.60^{+0.31}_{-0.31}$	$25.13^{+0.11}_{-0.11}$	$24.29^{+0.21}_{-0.20}$	–	$1.83^{+0.11}_{-0.11}$	$0.83^{+0.06}_{-0.06}$	$0.87^{+0.06}_{-0.05}$
W36	03:18:29.2	41:41:38.9	–	–	–	–	–	–	–
W40	03:18:33.3	41:40:55.9	$-15.00^{+0.13}_{-0.13}$	$23.93^{+0.05}_{-0.05}$	$23.38^{+0.09}_{-0.09}$	$1.36^{+0.28}_{-0.29}$	$1.39^{+0.04}_{-0.03}$	$0.64^{+0.03}_{-0.03}$	$0.72^{+0.02}_{-0.02}$
W41	03:18:33.6	41:41:58.3	$-14.97^{+0.32}_{-0.31}$	$24.50^{+0.13}_{-0.13}$	$22.05^{+0.30}_{-0.30}$	–	$1.57^{+0.11}_{-0.10}$	$1.74^{+0.09}_{-0.09}$	$0.94^{+0.03}_{-0.03}$
W56	03:18:48.1	41:14:02.2	$-13.83^{+0.19}_{-0.19}$	$24.71^{+0.08}_{-0.08}$	$24.39^{+0.12}_{-0.12}$	$1.52^{+0.67}_{-0.68}$	$1.15^{+0.04}_{-0.03}$	$0.48^{+0.04}_{-0.03}$	$0.74^{+0.03}_{-0.03}$
W59	03:18:54.3	41:15:28.9	$-14.71^{+0.09}_{-0.09}$	$23.65^{+0.04}_{-0.04}$	$23.07^{+0.07}_{-0.07}$	$1.31^{+0.29}_{-0.29}$	$0.97^{+0.02}_{-0.02}$	$0.66^{+0.02}_{-0.02}$	$0.88^{+0.02}_{-0.02}$
W80	03:19:39.2	41:13:43.5	–	–	–	–	–	–	–

Table 1 – *continued*

ID	α (J2000.0)	δ (J2000.0)	$M_{\rm F814W}$ (mag)	$\langle\mu\rangle_{\rm e,F814W}$ (mag/□″)	$\mu_{0,\rm F814W}$ (mag/□″)	F475W − F814W (mag)	$R_{\rm e}$ (kpc)	n	b/a
W83	03:19:47.4	41:44:08.8	$-13.37^{+0.31}_{-0.31}$	$24.89^{+0.13}_{-0.12}$	$24.36^{+0.22}_{-0.23}$	$1.24^{+0.59}_{-0.58}$	$1.00^{+0.05}_{-0.05}$	$0.63^{+0.07}_{-0.07}$	$0.75^{+0.05}_{-0.05}$
W84	03:19:49.7	41:43:42.4	$-13.97^{+0.20}_{-0.21}$	$23.82^{+0.09}_{-0.09}$	$22.64^{+0.19}_{-0.18}$	$1.29^{+0.39}_{-0.38}$	$0.81^{+0.03}_{-0.03}$	$1.03^{+0.06}_{-0.06}$	$0.74^{+0.03}_{-0.02}$
W87†	03:19:57.4	41:29:31.4	$-12.98^{+0.16}_{-0.16}$	$23.67^{+0.06}_{-0.06}$	$23.48^{+0.08}_{-0.09}$	$1.32^{+0.46}_{-0.45}$	$0.44^{+0.01}_{-0.01}$	$0.37^{+0.03}_{-0.02}$	$0.88^{+0.03}_{-0.03}$

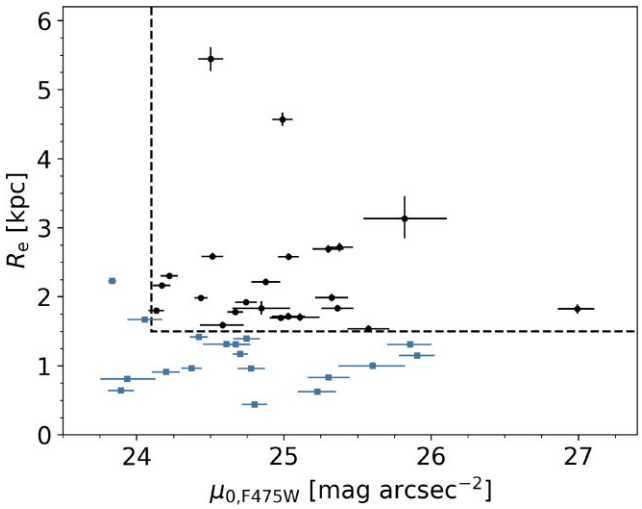

Figure 4. Half-light radii and central surface brightnesses for 41 Perseus cluster galaxies with both structural information and colours. $R_{\rm e}$ is the half-light radius along the major-axis from the F814W IMFIT model, and $\mu_{0,\rm F475W}$ is the central surface brightness in F475W, roughly equivalent to SDSS g. The dashed lines show the canonical UDG criteria of $R_{\rm e} > 1.5$ kpc and $\mu_{0,\rm F475W} > 24.1$ mag arcsec^{-2}. The 23 objects which pass the UDG criteria are plotted as black circles, while blue squares show the 18 that do not.

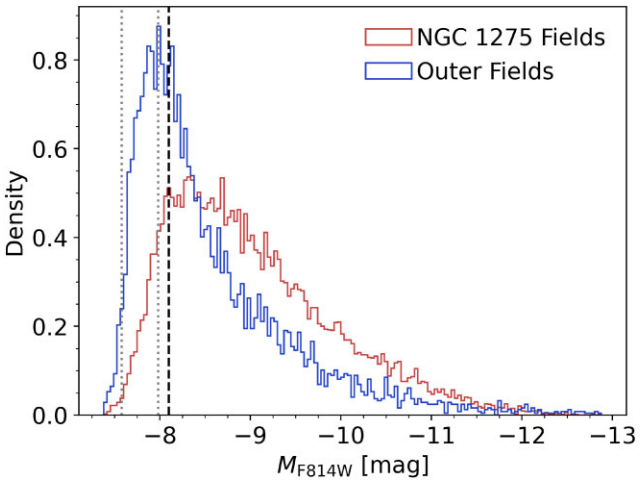

Figure 5. Normalized F814W luminosity functions of all GC candidates. The red histogram shows the GC candidates from the five NGC 1275 field pairs while the blue histogram are those from the outer fields. The dashed black line is the predicted turnover magnitude at $M_{\rm F814W} \approx -8.1$ (Miller & Lotz 2007). The GC catalogue is reasonably complete to the turnover magnitude as shown by the dotted grey lines which are the 50 per cent completeness limits of the most and least extincted fields.

2024) since they nudge up against the standard UDG criteria. Other galaxies in our sample are in the size–luminosity regime of classical dwarf spheroidals. Below, we will refer to the non-UDGs simply as 'dwarfs'. All galaxies in our Perseus sample can be considered as LSB galaxies.

Galaxy colours are measured on the model images within a 1 kpc diameter aperture. Our sample has an average F475W–F814W colour of ∼1.5, indicative of an old passive stellar population, though a small number of galaxies have bluer colours, e.g. R20 and R89 with F475W–F814W ∼ 1.0. For a more detailed discussion of the stellar populations of Perseus UDGs from spectroscopy, we refer the reader to Ferré-Mateu et al. (2023). Four of the five UDGs studied were found to be relatively old, metal-poor, and alpha-element enhanced.

Galaxy axis ratios hold potentially important clues to the intrinsic distribution of galaxy shapes. In Pfeffer et al. (2024), we investigate how GC richness varies with b/a for this sample of galaxies, as well as for UDGs in other environments.

3.2 GC system numbers

Our GC catalogue is reasonably complete in magnitude to the expected turnover of the GCLF of $M_{\rm F814W} \approx -8.1$ (Miller & Lotz 2007). Fig. 5 shows the magnitude distribution of all GC candidates from all *HST* pointings, split between the core NGC 1275 fields and the outer fields. The black dashed line shows the predicted turnover magnitude. The two-dotted grey lines are the 50 per cent completeness limits of the least and most extincted fields from the entire survey. We are thus mostly complete in magnitude at the turnover magnitude (i.e. completeness is between 71 per cent and 97 per cent, with a mean completeness of 87 per cent). The apparent brighter turnover of the NGC 1275 fields compared to the outer fields is expected given that the GC host galaxies tend to be giants in the core and dwarfs in the outer regions (Harris, Harris & Alessi 2013). However, extinction variation between fields also contributes.

Fig. 6 shows 12 × 12 kpc^2 (33 arcsec × 33 arcsec) F814W cutouts for all 50 sample galaxies. GC candidates are marked in red. The ID is shown in the upper right of each panel and the total number of GCs, including both the background and magnitude incompleteness corrections, is shown in the bottom right. Background-corrected values less than zero are shown as zero. The ID is bolded if the galaxy meets the strict definition of a UDG. Galaxies with IDs marked with † reside in the NGC 1275 core fields (R33, W74, and W87).

The cutouts reveal a variety of galaxy morphologies and GC system spatial distributions. For example, R25 is very faint but appears distorted, R89 has an S-shape which may indicate an interaction or it is perhaps a background spiral galaxy, as might be W84. W4 may have a bar. Both R21 and R84 have many GC candidates but the GC system of R84 appears to be more compact spatially. W6 appears to have a central nucleus but no corresponding GC system. Galaxies R79, W14, W29, W36, and W80 are all quite faint and a galaxy model could not be obtained.

A GC count for each galaxy was made by first counting the number of GC candidates in a fixed 15 kpc diameter circular aperture. Based on the GC system sizes (discussed later), such an aperture is expected to contain at least 90 per cent of a galaxy's GCs, and the use of a large

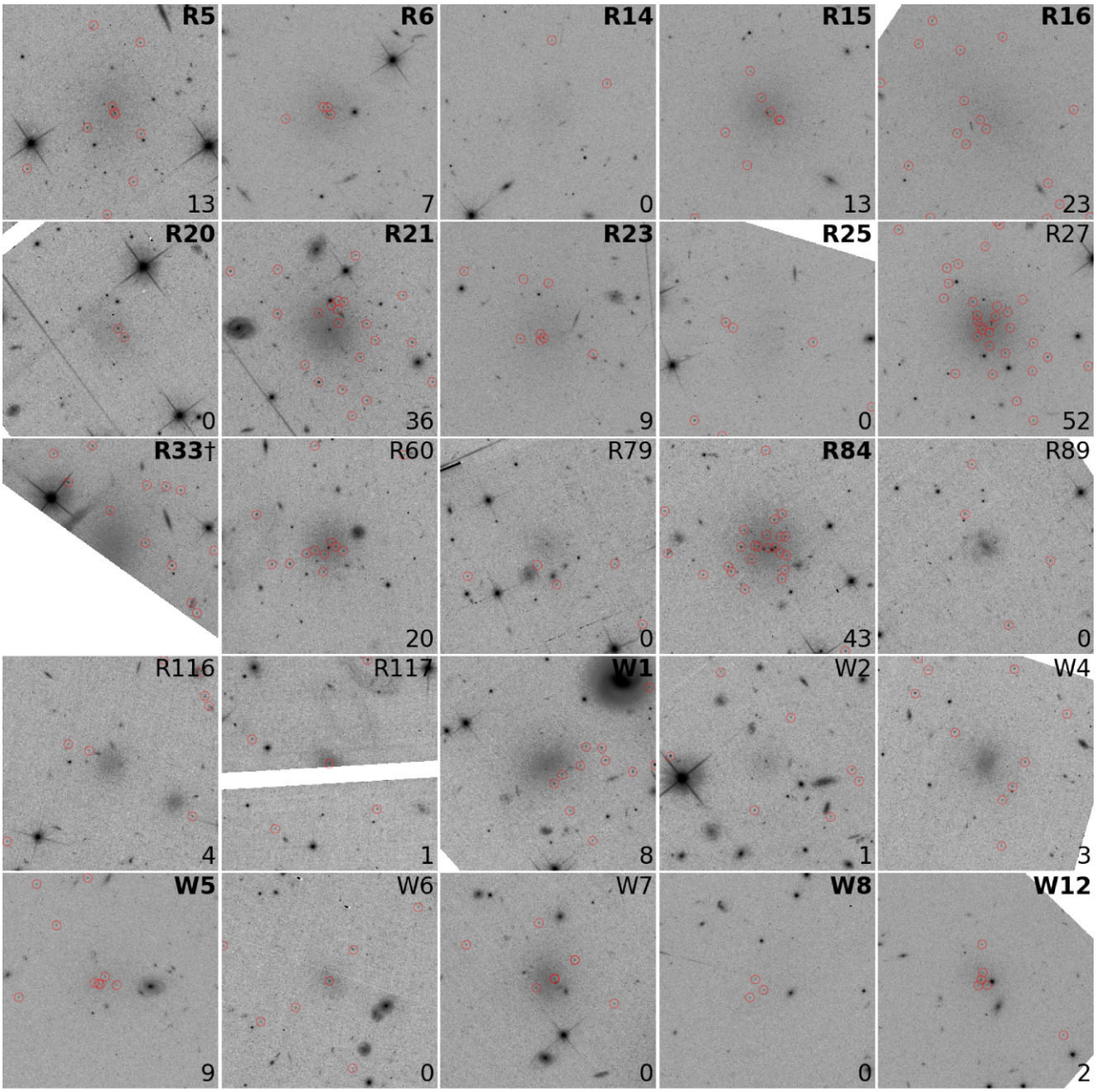

Figure 6. F814W postage stamps of all 50 LSB galaxies and their GC candidates. The cutouts are 12 × 12 kpc^2 (33 arcsec × 33 arcsec) at the adopted distance to the cluster. GC candidates are marked in red. Bold IDs denote galaxies that satisfy the strict UDG definition. The total number of GCs, after background and magnitude corrections, is shown in the bottom right. No GC number is shown for the three galaxies in the Perseus core fields near NGC 1275 (R33, W74, and W87) as the more detailed background modelling required for a GC assessment is saved for future work; the IDs for these galaxies are marked with †.

fixed-size aperture decouples the measure of GC numbers from the structural parameters of the galaxies[7]. We then make a correction for background contamination. The background density, and standard deviation, are estimated by counting sources that pass our GC cut in 500 similarly sized apertures placed randomly around each galaxy's respective image (but outside each galaxy's GC detection aperture). The expected number of background contaminants in the galaxy GC aperture, along with 1σ upper and lower numbers, are computed. The total number of GCs is then twice the background-corrected number of GCs, since our GCs only include those brighter than the GCLF turnover magnitude. We assume a symmetric universal GCLF that has a turnover magnitude of $M_{\rm TO,F814W} = -8.1$, noting that the GCLF of UDGs is still somewhat uncertain (e.g. Shen, van Dokkum & Danieli 2021; Janssens et al. 2022; Saifollahi et al. 2022), and that only NGC 5846_UDG1 has a near-complete GCLF measured so far (Danieli et al. 2022). The total GC number uncertainties are computed using the 1 sigma limits of background contaminants, where for simplicity we assume the uncertainty in the background dominates the error budget. Table 2 lists the total number of GCs for

[7]We repeated this procedure using an aperture three times the host galaxy half-light radius instead and found similar total GC counts for all galaxies, with the values agreeing within their uncertainties.

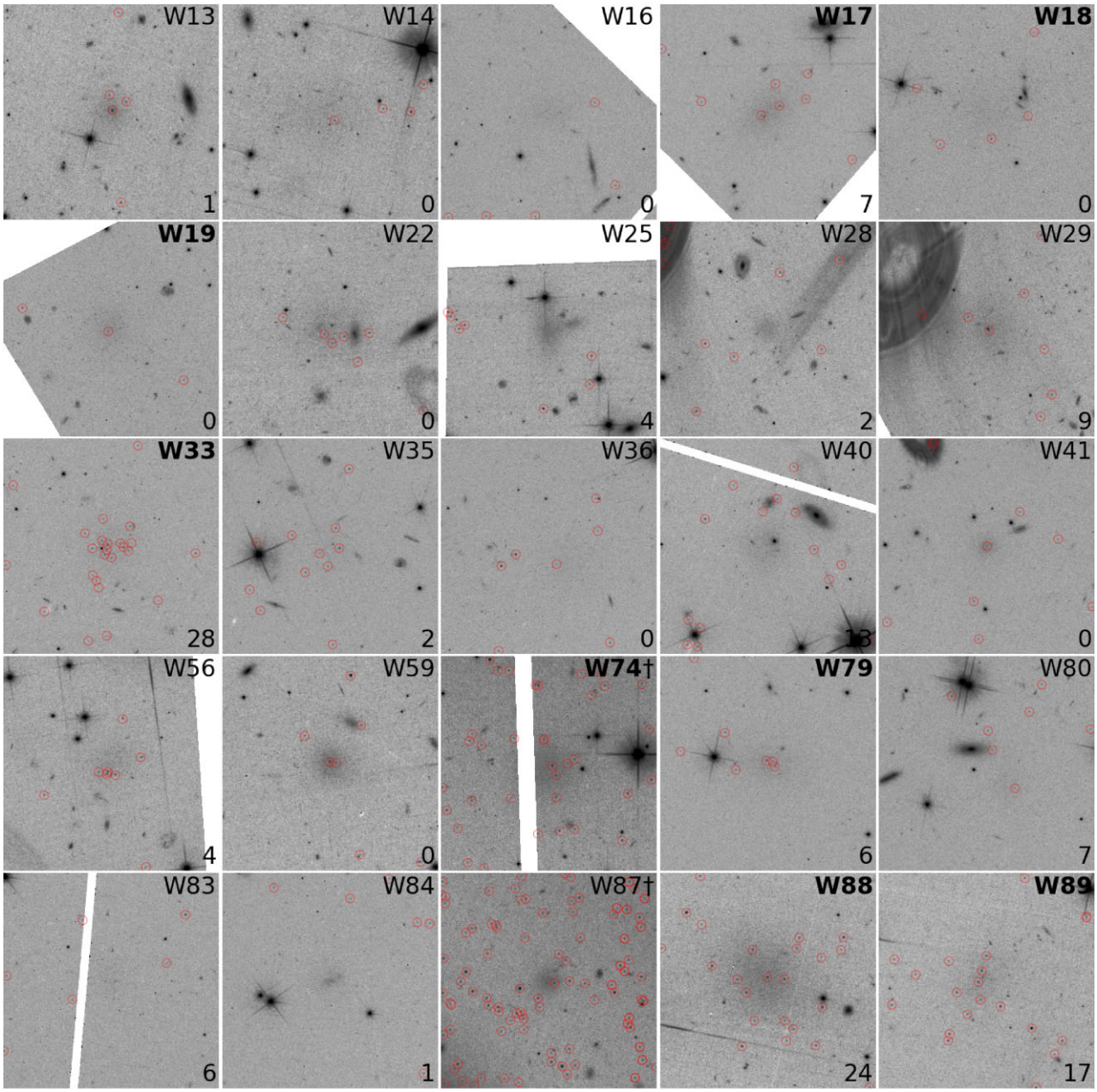

Figure 6. (*continued*)

the 42 galaxies that we were able to measure. Due to the complex and overwhelming density of GCs near NGC 1275, this analysis was not done for three galaxies in the NGC 1275 fields: R33, W74, and W87. These galaxies do not have $N_{\rm GC}$ values listed in Table 2 nor shown in Fig. 6. The more detailed background modelling necessary will be left for future work.

The mass of a GC system can be estimated using the total number of GCs and the typical GC mass, estimated using the GCLF turnover luminosity and a mass-to-light ratio. Using the FSPS code (Conroy et al. 2009; Conroy & Gunn 2010), adopting a simple stellar population (SSP), Chabrier (2003) initial mass function, $\log(Z/Z_{\odot}) = -1.5$ and an age of 8 Gyr we find a mass-to-light ratio of $M_{\star}/L_{\rm F814W} = 1.3$. For $M_{\rm TO,F814W} = -8.1$, the typical GC mass is then $\sim 1 \times 10^5$ M$_{\odot}$. Using this mass-to-light ratio for both the GC system and host galaxy, we calculate the ratio of the GC system mass to galaxy stellar mass and include it as a percentage in Table 2.

Fig. 7 shows the number of GCs as a function of galaxy F814W luminosity, and directly compares them to UDGs in the Coma cluster. As before, black circles are Perseus galaxies from our sample that meet the UDG criteria, and blue squares are UDG-like galaxies that we designate as dwarfs. GC counts for Coma UDGs (grey symbols) are from Forbes et al. (2020), who combined literature values from van Dokkum et al. (2017), Lim et al. (2018), and Amorisco et al. (2018). The Coma cluster UDGs have been converted from V-band luminosities to F814W assuming $V - I = 1$. The dotted lines show the GC system mass to host galaxy stellar mass with both assuming $M_{\star}/L_{\rm F814W} = 1.3$. From bottom to top are plotted GC mass fractions of 0.4 per cent, 1 per cent, and 5 per cent.

Table 2. Globular cluster properties of PIPER LSBs. $M_{\rm GC}/M_\star$ is the ratio of GC system mass to galaxy stellar mass. $R_{\rm GC}$ is the half-number radius of the GC system. $R_{\rm GC}/R_{\rm e,c}$ is the ratio of GC system to host galaxy (circularized) size. ⟨F475W–F814W⟩ is the mean colour of the GCs. The last column shows the results of a visual determination of the presence of a stellar nucleus. R33, W74, and W87 reside in the NGC 1275 core fields where no GC assessment was performed, and are marked with a †.

ID	$N_{\rm GC}$	$M_{\rm GC}/M_\star$	$R_{\rm GC}$ (kpc)	$R_{\rm GC}/R_{\rm e,c}$	⟨F475W − F814W⟩ (mag)	Nucleated
R5	13 ± 6	$1.0\%^{+0.6}_{-0.5}$	$2.9^{+1.0}_{-0.7}$	$1.2^{+0.4}_{-0.3}$	1.68 ± 0.07	No
R6	7 ± 1	$0.5\%^{+0.1}_{-0.1}$	–	–	–	No
R14	-1 ± 5	$0.0\%^{+0.0}_{-0.0}$	–	–	–	No
R15	13 ± 5	$0.5\%^{+0.2}_{-0.2}$	$2.6^{+1.0}_{-0.7}$	$1.2^{+0.5}_{-0.3}$	1.35 ± 0.03	Yes
R16	23 ± 7	$0.5\%^{+0.2}_{-0.2}$	$3.7^{+0.9}_{-0.7}$	$1.0^{+0.3}_{-0.2}$	1.61 ± 0.04	No
R20	-2 ± 8	$0.0\%^{+0.0}_{-0.0}$	–	–	–	No
R21	36 ± 8	$1.7\%^{+0.5}_{-0.4}$	$3.1^{+0.6}_{-0.5}$	$1.5^{+0.3}_{-0.3}$	1.51 ± 0.03	Yes
R23	9 ± 6	$0.4\%^{+0.3}_{-0.3}$	$2.5^{+1.1}_{-0.7}$	$1.0^{+0.5}_{-0.3}$	1.56 ± 0.05	No
R25	-8 ± 11	$0.0\%^{+0.0}_{-0.0}$	–	–	–	No
R33†	–	–	–	–	–	No
R84	43 ± 6	$2.2\%^{+0.5}_{-0.4}$	$2.2^{+0.4}_{-0.3}$	$1.2^{+0.2}_{-0.2}$	1.45 ± 0.03	No
W1	8 ± 10	$0.6\%^{+0.8}_{-0.6}$	$3.9^{+1.9}_{-1.2}$	$2.4^{+1.2}_{-0.8}$	1.57 ± 0.09	No
W5	9 ± 7	$1.2\%^{+1.2}_{-0.9}$	$3.4^{+1.4}_{-0.9}$	$2.0^{+0.9}_{-0.6}$	1.36 ± 0.07	No
W8	-0 ± 7	$0.0\%^{+0.0}_{-0.0}$	–	–	–	No
W12	2 ± 7	$0.2\%^{+1.1}_{-0.2}$	–	–	–	No
W17	7 ± 6	$0.8\%^{+0.9}_{-0.7}$	$3.8^{+1.8}_{-1.1}$	$2.5^{+1.3}_{-0.8}$	1.72 ± 0.14	No
W18	-4 ± 9	$0.0\%^{+0.0}_{-0.0}$	–	–	–	No
W19	-5 ± 6	$0.0\%^{+0.0}_{-0.0}$	–	–	–	No
W33	28 ± 12	$4.7\%^{+3.1}_{-2.4}$	$2.4^{+0.5}_{-0.4}$	$1.5^{+0.4}_{-0.3}$	1.30 ± 0.03	No
W74†	–	–	–	–	–	No
W79	6 ± 8	$0.6\%^{+1.0}_{-0.6}$	–	–	–	No
W88	24 ± 13	$0.4\%^{+0.3}_{-0.3}$	$3.5^{+0.8}_{-0.6}$	$0.8^{+0.2}_{-0.2}$	1.64 ± 0.07	No
W89	17 ± 14	$3.4\%^{+3.8}_{-2.9}$	$4.0^{+1.2}_{-0.9}$	$2.6^{+0.9}_{-0.7}$	1.42 ± 0.08	No
R27	52 ± 8	$1.3\%^{+0.2}_{-0.2}$	$2.4^{+0.4}_{-0.3}$	$1.1^{+0.2}_{-0.2}$	1.44 ± 0.02	No
R60	20 ± 6	$2.0\%^{+0.8}_{-0.7}$	$2.6^{+0.7}_{-0.5}$	$1.9^{+0.5}_{-0.4}$	1.37 ± 0.05	Yes
R79	-4 ± 9	–	–	–	–	Yes
R89	-1 ± 7	$0.0\%^{+0.0}_{-0.0}$	–	–	–	No
R116	4 ± 8	$1.2\%^{+2.4}_{-1.2}$	–	–	–	No
R117	1 ± 8	$0.3\%^{+2.4}_{-0.3}$	–	–	–	Yes
W2	1 ± 10	$0.1\%^{+3.0}_{-0.1}$	–	–	–	Yes
W4	3 ± 12	$0.3\%^{+1.5}_{-0.3}$	–	–	–	No
W6	-2 ± 10	$0.0\%^{+0.0}_{-0.0}$	–	–	–	Yes
W7	0 ± 10	$0.0\%^{+1.8}_{-0.0}$	–	–	–	No
W13	1 ± 7	$0.2\%^{+2.0}_{-0.2}$	–	–	–	Yes
W14	-1 ± 7	–	–	–	–	No
W16	-2 ± 7	$0.0\%^{+0.0}_{-0.0}$	–	–	–	No
W22	-2 ± 8	$0.0\%^{+0.0}_{-0.0}$	–	–	–	No
W25	4 ± 6	$0.8\%^{+1.6}_{-0.8}$	–	–	–	No
W28	2 ± 9	$1.9\%^{+9.3}_{-1.9}$	–	–	–	No
W29	9 ± 9	–	$4.4^{+1.8}_{-1.2}$	–	1.83 ± 0.13	Yes
W35	2 ± 11	$0.6\%^{+3.8}_{-0.6}$	–	–	–	No
W36	-6 ± 12	–	–	–	–	No
W40	13 ± 10	$2.2\%^{+2.3}_{-1.8}$	$3.9^{+1.4}_{-1.0}$	$3.3^{+1.3}_{-0.9}$	1.94 ± 0.12	No
W41	-1 ± 12	$0.0\%^{+0.0}_{-0.0}$	–	–	–	No
W56	4 ± 8	$1.9\%^{+5.2}_{-1.9}$	–	–	–	No
W59	0 ± 9	$0.1\%^{+2.3}_{-0.1}$	–	–	–	Yes
W80	7 ± 8	–	$4.3^{+2.0}_{-1.3}$	–	1.29 ± 0.10	No

Table 2 – *continued*

ID	$N_{\rm GC}$	$M_{\rm GC}/M_\star$	$R_{\rm GC}$ (kpc)	$R_{\rm GC}/R_{\rm e,c}$	⟨F475W − F814W⟩ (mag)	Nucleated
W83	6 ± 7	$4.5\%^{+8.7}_{-4.5}$	–	–	–	No
W84	1 ± 7	$0.3\%^{+3.8}_{-0.3}$	–	–	–	No
W87†	–	–	–	–	–	No

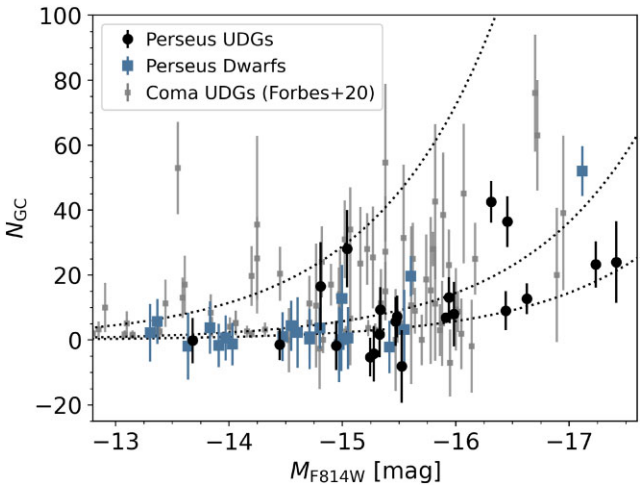

Figure 7. Total number of GCs ($N_{\rm GC}$) as a function of galaxy absolute magnitude. Black circles are galaxies which satisfy the UDG criteria, blue squares are other LSB dwarfs. The dotted curves show GC system mass to stellar mass fractions assuming a mass-to-light ratio of $M_\star/L_{\rm F814W} = 1.3$ for both. From bottom to top, the curves show mass fractions of 0.4 per cent, 1 per cent, and 5 per cent. For comparison, we also show $N_{\rm GC}$ for Coma UDGs from Forbes et al. 2020 in grey. The Perseus cluster reveals some UDGs with rich GC systems ($N_{\rm GC} > 20$).

The plot shows that a few Perseus UDGs are GC rich, hosting many tens of GCs, as is found in the Coma cluster. Given the general lack of rich GC systems in other clusters (Fornax, Virgo, Hydra I) this may suggest that only the most massive ($M_{200} \sim 10^{15}$ M$_\odot$) clusters host GC rich UDGs. We note R21 with 36 ± 8 and R84 with 43 ± 6 GCs. The richest GC system belongs to R27, which is slightly brighter than the standard UDG definition, with 52 ± 8 GCs. The GC system mass fractions for Perseus cluster LSB galaxies are generally consistent with a 0.4 per cent mass fraction, with the highest being the UDG W33 with a 4.7 per cent mass fraction. Coma cluster LSB dwarfs reveal a similar range in GC to galaxy mass fractions up to a maximum of 5 per cent (with a couple of exceptions). These ratios can be compared to the Milky Way halo which has a ratio of 1–2 per cent (Harris, Blakeslee & Harris 2017; Deason, Belokurov & Sanders 2019). Although our Perseus UDG sample and the Coma UDGs reveal similar GC to galaxy mass fractions (and possibly higher on average for Coma), the Perseus galaxies are on average more luminous (higher mass) than the Coma UDG sample from Forbes et al. (2020) and there may be other selection effects that should be considered. For example, a weak correlation for GC-rich UDGs to lie at smaller clustercentric distances is expected (Buzzo et al. 2024). However, this is hard to probe with our data set as all our UDGs lie at relatively small projected clustercentric distances, with the most distant galaxy at ∼750 kpc or ∼$0.4 \times R_{200}$. Moreover, many bright galaxies in the core of Perseus are arranged in a near-linear feature to the southwest of NGC 1275, and it is possible that the distance to this filament is the driver of any local environmental effects.

If we separate our Perseus sample into UDGs and dwarfs, we find that the mean number of GCs hosted by UDGs is 11 ± 3 whereas the dwarfs host an average of only 4 ± 2 GCs. However, in terms of GC system mass to galaxy stellar mass, this difference vanishes with both the UDGs and dwarfs hosting a similar mean mass fraction. Re-examining Fig. 4 provides a possible explanation: due to the degeneracy between effective radius, luminosity, and Sérsic index, a size cut (i.e. the UDG $R_{\rm e} > 1.5$ kpc definition) in a population of galaxies with similar surface brightnesses and Sérsic indices ($n \sim 1$) is equivalent to a luminosity cut, and to a stellar mass cut assuming similar mass-to-light ratios. This is reflected in Fig. 7 where most Perseus galaxies brighter than $M_{\rm F814W} = -15$ are UDGs, whereas those fainter are dwarfs.

3.3 GC system sizes

In order to measure the sizes of GC systems, we employ an alternative process for removing background contaminants. We start with all the GC candidates within a radius $r = 7.5$ kpc of each galaxy. For each galaxy, the number of expected background contaminants was estimated in the same way as described above. A background sample of sources that meet the GC criteria is then randomly drawn from elsewhere in each galaxy's image. For each background source, we then removed the galaxy GC candidate nearest in Euclidean distance on the colour–magnitude diagram. The result of this process is shown in Fig. 8. Each CMD shows all the GC candidates within $r < 7.5$ kpc. Blue × symbols are candidates that were removed as background objects, and black points are those that survived this process.[8] For comparison, the red dotted line shows the mean colour of the host galaxy, though it is absent in the cases where IMFIT did not converge in at least one of the bands.

A Sérsic model was then fitted to the one dimensional radial distribution of GC candidates after background removal using the EMCEE package (Foreman-Mackey et al. 2013). The only free parameter is the 'effective' radius – which for GCs we will refer to as the half-number radius $R_{\rm GC}$. The ellipticity of the GC system is fixed to zero. The Sérsic index n was initially allowed to vary. For the richest six GC systems with $N_{\rm GC} > 20$ (i.e. at least 10 candidates), we found a mean n of 1.1 ± 0.1, and subsequently we fixed it to $n = 1$. The best-fitting $R_{\rm GC}$ is the 50 per cent percentile from the posterior distribution, with 16 per cent and 84 per cent uncertainties. The 16 per cent, 50 per cent, and 84 per cent percentiles from the $R_{\rm GC}$ posterior distribution is recorded.

The background removal and EMCEE fitting was then repeated 25 times for each galaxy (Fig. 8 is showing one realization). We adopt the mean 50 per cent $R_{\rm GC}$ percentile from the 25 fits as the

[8]Fig. 8 provides a sanity check on the $N_{\rm GC}$ values in Table 2. Twice the number of black points (as only the bright half of the GCLF is selected and plotted) agree with the total numbers for each galaxy.

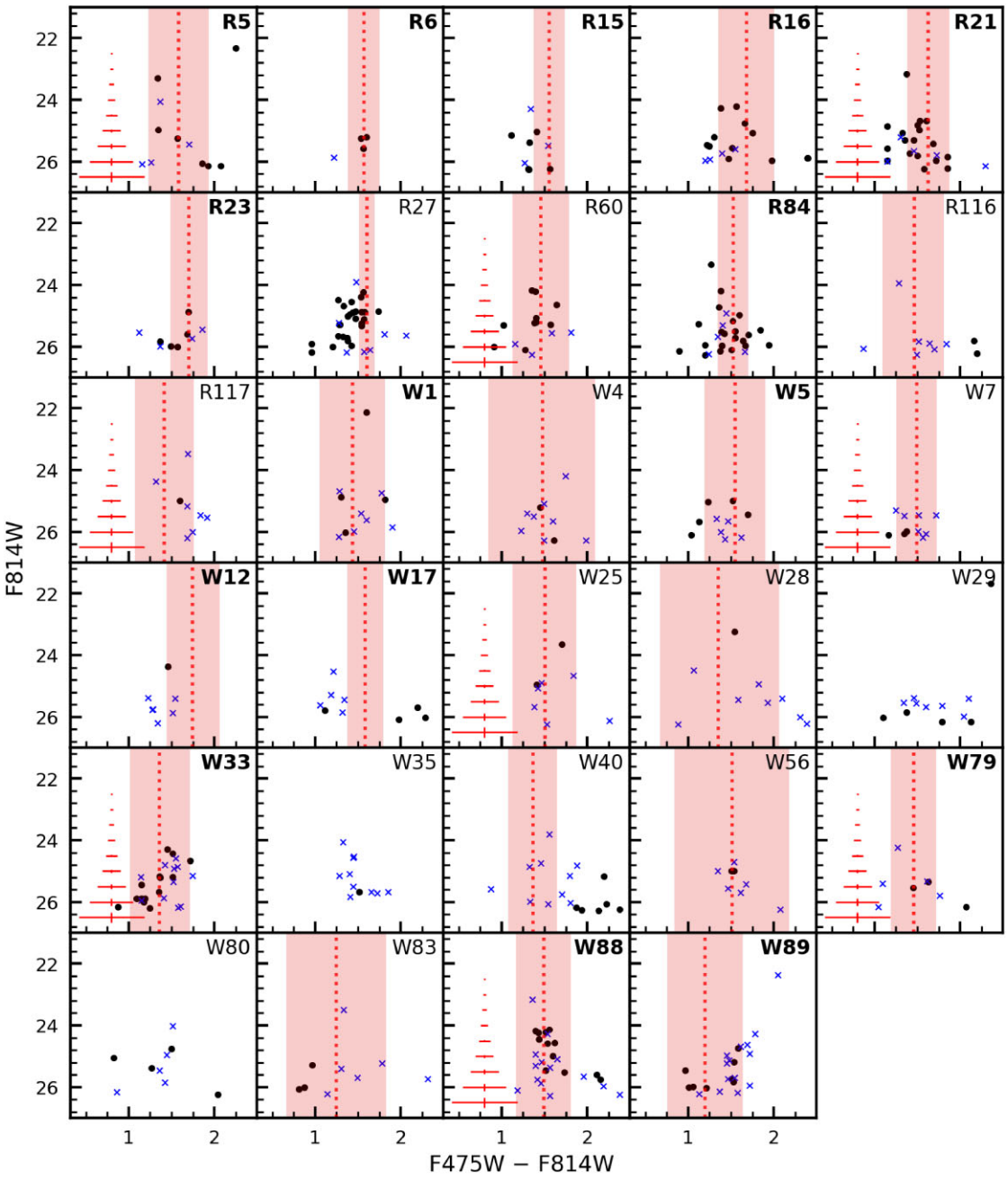

Figure 8. Colour–magnitude diagrams of point sources around target galaxies with GC counts above the expected background contribution. A statistical background correction was made, removing GC candidates nearest in colour and magnitude (see the text for details). GC candidates that survived the correction are shown in black and those that were removed are the blue crosses. Bold IDs denote galaxies that satisfy the strict UDG definition. LSBs in the core of the Perseus cluster are also not shown. The host galaxy colour is shown as the dotted red vertical line and the shaded band is the colour uncertainty; it is absent if the IMFIT result is unreliable. Characteristic error bars derived from the artificial star tests are shown on the right side of a subset of panels. Many of the GC systems have colours similar to the colour of the host galaxy.

final $R_{\rm GC}$ value, with the mean 16 per cent and 84 per cent percentiles as uncertainties. Table 2 lists the resulting half-number radii ($R_{\rm GC}$) in kpc and the ratio of GC system size to galaxy half-light radius ($R_{\rm GC}/R_{\rm e,c}$). The $R_{\rm GC}$ posterior distributions will not all overlap when there are fewer than 4 GC candidates (after background removal), and so $R_{\rm GC}$ and $R_{\rm GC}/R_{\rm e,c}$ values are not reported in such cases.

As few as 4 GC candidates will still provide a reliable $R_{\rm GC}$ estimate. This was tested on R27 (the galaxy with the richest GC system in our sample) by re-performing the EMCEE fit 25 times with a randomly selected subset of 4 of its 26 candidates. A majority of the fits agree within uncertainties with the $2.4^{+0.4}_{-0.3}$ kpc estimate, and the mean percentiles overlap.

As noted in the Introduction, the number of GCs around UDGs in the Coma cluster has been the subject of recent debate with much lower GC numbers claimed by Saifollahi et al. (2022) for six Coma UDGs. A key factor in the different GC numbers found with previous studies is the smaller half-number radii for GC systems found by Saifollahi et al. (2022). For example, for DF44 and DFX1,

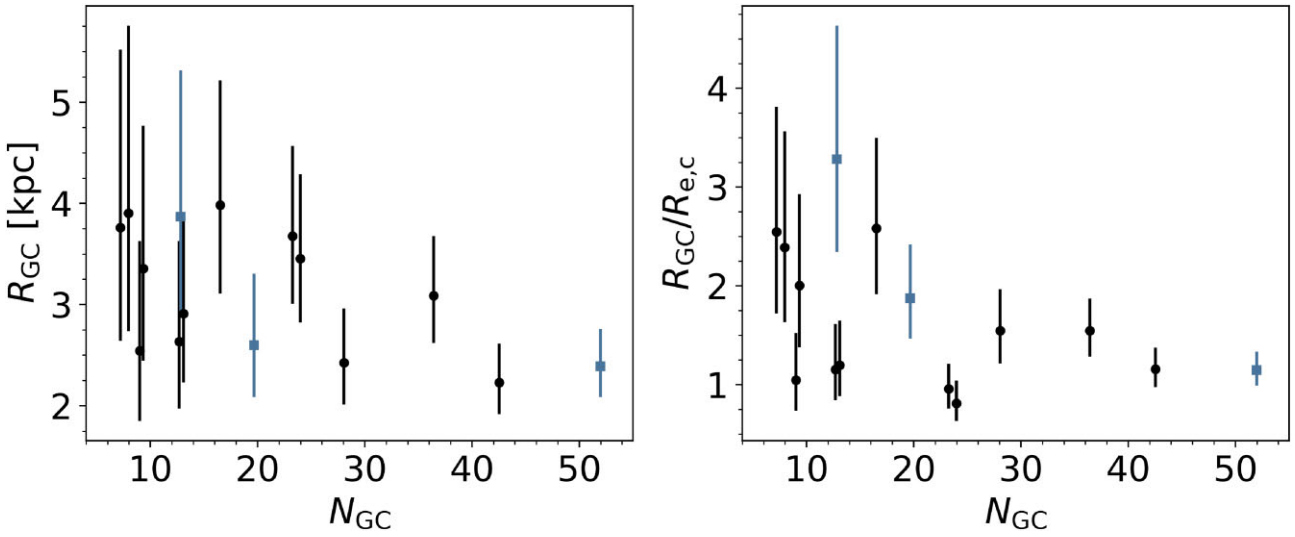

Figure 9. *Left*: GC system half-number radius as a function of number of GCs. *Right*: Ratio of GC half number radius to circularized galaxy half light radius plotted against number of GCs. Galaxies with the richest GC systems ($N_{GC} > 20$) have R_{GC}/R_e ratios of ∼1.2. In both panels, only galaxies with at least three GC candidates are included. Black circles are galaxies which satisfy the UDG criteria, blue squares are dwarfs.

van Dokkum et al. (2017) found $R_{GC}/R_e = 1.5$ whereas Saifollahi et al. (2022) found $R_{GC}/R_e \sim 0.8$ for both.

In Fig. 9, we show both R_{GC} and R_{GC}/R_e versus the number of GCs for systems with more than 3 GCs. In both panels, we find a broad scatter, particularly for galaxies with low numbers of GCs. For those with rich GC systems ($N_{GC} > 20$) the average half-number radius is ∼3 kpc and R_{GC}/R_e ratios is ∼1.2. Many galaxies have a similar size ratio to that found by van Dokkum et al. (2017) for DF44 and DFX1 in the Coma cluster. See Forbes & Gannon (2024) for a more detailed discussion of Coma cluster UDGs and the role of the GC system size in determining the total number of GCs.

3.4 GC system colours

We computed mean GC colours after background contaminants were statistically removed using the same background removal process described above to measure GC system sizes. Here, too the process was repeated 25 times for each galaxy, and we require a minimum of 4 GC candidates (after background removal) to measure a mean colour. The adopted mean GC colour is the average value of the 25 sample means, with the uncertainty being the standard deviation of the means. The mean GC colours are listed in the sixth column of Table 2.

In Fig. 10, we show the difference between the colour of each galaxy and the mean colour of its GC system. A positive colour differential value signifies that the galaxy is redder than its GCs (as found for DF2 and DF4 in the NGC 1052 group by van Dokkum et al. 2022), indicating a more extended star formation history with metal enrichment. The dotted red line and red shaded area show the weighted mean colour difference and the weighted error of the mean, respectively. We find a mean colour difference of $\Delta(\text{F475W–F814W})_{\text{UDG–GCS}} = 0.07 \pm 0.08$ mag. Thus we find a slight positive difference but statistically they have the same colour in the mean. Furthermore, each individual galaxy, except for one outlier, has GC colours consistent with their host galaxy. In a detailed study of the field UDG DGSAT I, Janssens et al. (2022) found identical colours for the GCs and underlying galaxy light. Saifollahi et al. (2022) also compared the F475W–F814W colours of six Coma

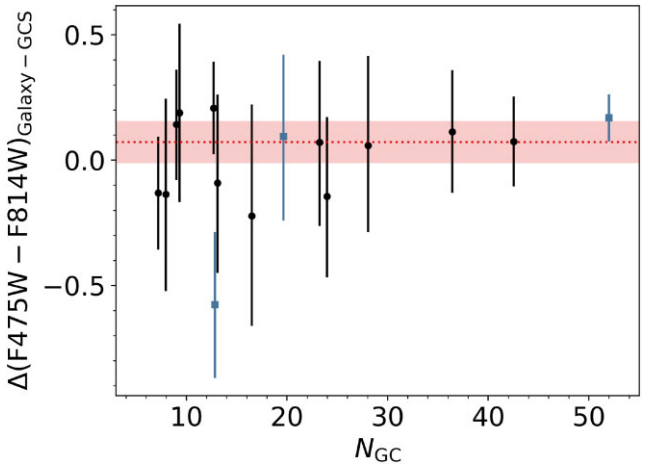

Figure 10. Colour difference between host galaxy and the mean colour of its GC system plotted against GC number. Black circles are galaxies which satisfy the UDG criteria, blue squares are dwarfs. Positive values indicate galaxies that are redder than their GCs. The dotted red line and shaded area are the weighted mean colour difference and the weighted error of the mean, respectively, equal to $\Delta(\text{F475W–F814W})_{\text{UDG–GCS}} = 0.07 \pm 0.08$ mag. Within the uncertainty, galaxies and GC systems have the same mean colour indicating the same age and metallicity for their stars.

cluster UDGs with their GC systems finding similar colours. These observations are compatible with a scenario whereby the galaxies are composed of the *same* stellar populations (a combination of age and metallicity) as their GCs.

Very few UDGs have spectroscopic age and metallicity measures for both the galaxy stars and the GCs. One such case is NGC 5846_UDG1 (which is discussed in detail by Forbes & Gannon 2024). Using MUSE on the VLT, Müller et al. (2020) found the same ages and metallicities, within the uncertainties, for the galaxy stars and a dozen of the brightest GCs. Another is NGC 1052-DF2, where Fensch et al. (2019) found the same ages, but GCs with lower metallicity than the galaxy stars. As noted in the Introduction, UDGs made up of stars that have the same mean ages and metallicities as

their GCs are good candidates for 'failed galaxies'. In this scenario, early quenching of the galaxy stars prevents extended star formation. Over time, GCs are disrupted and their stars contribute, and perhaps dominate over, the original galaxy stars.

3.5 Nucleation

A quick assessment for the presence of stellar nuclei was performed by eye and the results from this are listed in the last column of Table 2. In some cases, the same central object is classified as a GC candidate in our automated detection process as well as a stellar nucleus in our visual inspection. This highlights the arbitrary nature of determining whether a near-centrally located object is a *bona fide* GC or a true nucleus (which itself may have been formed by the merger of GCs). We find 10 of our sample galaxies possess a clear stellar nucleus, a frequency of about 20 per cent. This fraction is similar to that found by Lim et al. (2018) for UDGs in the outer regions of the Coma cluster, and about half the frequency of UDGs located in the Coma cluster core. Selection effects need to be taken into account for a detailed comparison.

We have previously postulated (Janssens et al. 2019) that the destruction of nucleated UDGs in clusters may be an important pathway towards the formation of ultra-compact dwarfs (UCDs). UCDs have sizes and luminosities similar to those of stellar nuclei (which may themselves be the merged product of several GCs). The disruption of the surrounding galaxy by tidal forces is expected to leave only the dense nucleus, which is then identified as a UCD (Pfeffer & Baumgardt 2013). This process has recently received confirmation by observation of some transition objects between UDGs and UCDs in the Virgo cluster (Wang et al. 2023).

4 SUMMARY AND CONCLUSIONS

As part of the PIPER survey of the Perseus cluster, we have conducted an analysis of an initial sample of 50 low-surface brightness (LSB) galaxies identified in ground-based imaging. Our new data from the *Hubble Space Telescope* consists of F475W and F814W images with the ACS camera, along with F475X and F814W images with the WFC3 camera covering all 50 galaxies. We were able to measure the structural parameters and colours for 41 galaxies, finding that 23 meet the traditional criteria for a UDG. The remaining 18 galaxies have UDG-like properties, having either a slightly brighter surface brightness and/or a more compact size than the standard definition. As well as measuring surface brightnesses and half-light radii, we measure total magnitudes, ellipticities, Sérsic indices and mean colours for the galaxies.

We identify globular cluster (GC) candidates associated with each galaxy. After corrections for background contamination and magnitude incompleteness, we estimate the total number of GCs hosted by each galaxy. We also measure their mean colour and their spatial extent as quantified by the radius enclosing half of the total number.

Although most galaxies have few, if any, GCs we find some to reveal GC systems with tens of GCs. These GC-rich UDGs rival those seen in the Coma cluster. Given the general lack of rich GC systems in other clusters (Fornax, Virgo, Hydra I) this may suggest that only the most massive ($M_{200} \sim 10^{15}$ M$_\odot$) clusters host GC-rich UDGs. We also find that the GC system mass to galaxy stellar mass ratio is similar for Perseus cluster LSB galaxies compared to those in the Coma cluster.

We find that the GC systems of our Perseus LSB galaxies with rich GC systems ($N_{GC} > 20$) have an extent that is typically around 1.2 times that of their host galaxy half-light radius. This is similar to that found for well-studied GC rich UDGs in the Coma cluster by van Dokkum et al. (2017).

The mean colour of our GC systems is the same as that of the host galaxies within our measurement uncertainty, i.e. 0.07 ± 0.08 mag. This suggests that GCs and galaxy stars may have formed at the same epoch from the same enriched gas. This would be expected in the 'failed galaxy' formation scenario for UDGs where star formation is quenched early and subsequent disruption of GCs makes a significant contribution to the stellar component of the host UDG.

ACKNOWLEDGEMENTS

We thank the anonymous referee for suggestions which improved the quality of the manuscript, and B. Koribalski, L. Buzzo and L. Haacke for useful discussions. This research is based on observations made with the NASA/ESA *Hubble Space Telescope* for program GO-15235 and obtained at the Space Telescope Science Institute (STScI). STScI is operated by the Association of Universities for Research in Astronomy, Inc., under NASA contract NAS 5–26555. Support for this program was provided by NASA through grants to AJR and PRD from STScI. AJR was supported by National Science Foundation grant AST-2308390. This research made use of Astropy,[9] a community-developed core PYTHON package for Astronomy (ASTROPY Collaboration et al. 2013, 2018). This research made use of Photutils, an ASTROPY package for detection and photometry of astronomical sources (Bradley et al. 2021). This research has made use of the NASA/IPAC Extragalactic Database (NED), which is operated by the Jet Propulsion Laboratory, California Institute of Technology, under contract with the National Aeronautics and Space Administration. This research has made use of NASA's Astrophysics Data System Bibliographic Services.

DATA AVAILABILITY

The raw *HST* data can be obtained from MAST. For other data, reasonable requests will be considered by the first author.

REFERENCES

Aguerri J. A. L., Girardi M., Agulli I., Negri A., Dalla Vecchia C., Domínguez Palmero L., 2020, MNRAS, 494, 1681
Amorisco N. C., Monachesi A., Agnello A., White S. D. M., 2018, MNRAS, 475, 4235
Astropy Collaboration et al., 2013, A&A, 558, A33
Astropy Collaboration et al., 2018, AJ, 156, 123
Bertin E., Arnouts S., 1996, A&AS, 117, 393
Bohlin R. C., 2016, AJ, 152, 60
Bradley L. et al., 2021, astropy/photutils: 1.0.2
Buzzo M. L. et al., 2024, MNRAS, 529, 3210
Chabrier G., 2003, PASP, 115, 763
Conroy C., Gunn J. E., 2010, ApJ, 712, 833
Conroy C., Gunn J. E., White M., 2009, ApJ, 699, 486
Danieli S. et al., 2022, ApJ, 927, L28
Deason A. J., Belokurov V., Sanders J. L., 2019, MNRAS, 490, 3426
Deustua S. E., Mack J., 2018, Comparing the ACS/WFC and WFC3/UVIS Calibration and Photometry, Space Telescope WFC Instrument Science Report
Erwin P., 2015, ApJ, 799, 226
Evstigneeva E. A. et al., 2008, AJ, 136, 461
Fensch J. et al., 2019, A&A, 625, A77

[9] http://www.astropy.org

Ferré-Mateu A., Gannon J. S., Forbes D. A., Buzzo M. L., Romanowsky A. J., Brodie J. P., 2023, MNRAS, 526, 4735
Forbes D. A., Gannon J., 2024, MNRAS, 528, 608
Forbes D. A., Alabi A., Romanowsky A. J., Brodie J. P., Arimoto N., 2020, MNRAS, 492, 4874
Foreman-Mackey D., Hogg D. W., Lang D., Goodman J., 2013, PASP, 125, 306
Gannon J. S. et al., 2022, MNRAS, 510, 946
Graham A. W., Driver S. P., 2005, PASA, 22, 118
Gwyn S. D. J., 2008, PASP, 120, 212
Harris W. E., Harris G. L. H., Alessi M., 2013, ApJ, 772, 82
Harris W. E., Blakeslee J. P., Whitmore B. C., Gnedin O. Y., Geisler D., Rothberg B., 2016, ApJ, 817, 58
Harris W. E., Blakeslee J. P., Harris G. L. H., 2017, ApJ, 836, 67
Harris W. E. et al., 2020, ApJ, 890, 105
Ho M., Ntampaka M., Rau M. M., Chen M., Lansberry A., Ruehle F., Trac H., 2022, Nat. Astron., 6, 936
Janssens S. R., Abraham R., Brodie J., Forbes D. A., Romanowsky A. J., 2019, ApJ, 887, 92
Janssens S. R. et al., 2022, MNRAS, 517, 858
King I., 1962, AJ, 67, 471
La Marca A. et al., 2022, A&A, 665, A105
Li D. D. et al., 2022, ApJ, 935, 3
Lim S., Peng E. W., Côté P., Sales L. V., den Brok M., Blakeslee J. P., Guhathakurta P., 2018, ApJ, 862, 82
Lim P. L. et al., 2020a, ACStools: Python tools for Hubble Space Telescope Advanced Camera for Surveys data, Astrophysics Source Code Library, ascl:2011.024
Lim S. et al., 2020b, ApJ, 899, 69
Miller B. W., Lotz J. M., 2007, ApJ, 670, 1074
Müller O. et al., 2020, A&A, 640, A106
Peng C. Y., Ho L. C., Impey C. D., Rix H.-W., 2002, AJ, 124, 266
Pfeffer J., Baumgardt H., 2013, MNRAS, 433, 1997
Pfeffer J. et al., 2024, MNRAS, 529, 4914
Prole D. J. et al., 2019, MNRAS, 484, 4865
STScI Development Team, 2020, stsynphot: synphot for HST and JWST, Astrophysics Source Code Library, ascl:2010.003
Saifollahi T., Zaritsky D., Trujillo I., Peletier R. F., Knapen J. H., Amorisco N., Beasley M. A., Donnerstein R., 2022, MNRAS, 511, 4633
Schlafly E. F., Finkbeiner D. P., 2011, ApJ, 737, 103
Shen Z., van Dokkum P., Danieli S., 2021, ApJ, 909, 179
Simionescu A. et al., 2011, Science, 331, 1576
Sirianni M. et al., 2005, PASP, 117, 1049
Stetson P. B., 1987, PASP, 99, 191
Wang K. et al., 2023, Nature, 623, 296
Wittmann C. et al., 2017, MNRAS, 470, 1512
van Dokkum P. G., Abraham R., Merritt A., Zhang J., Geha M., Conroy C., 2015, ApJ, 798, L45
van Dokkum P. et al., 2017, ApJ, 844, L11
van Dokkum P. et al., 2022, ApJ, 940, L9

APPENDIX A: COMPLETENESS CURVES

In Fig. A1, we show the F814W artificial star completeness curves for all 30 fields.

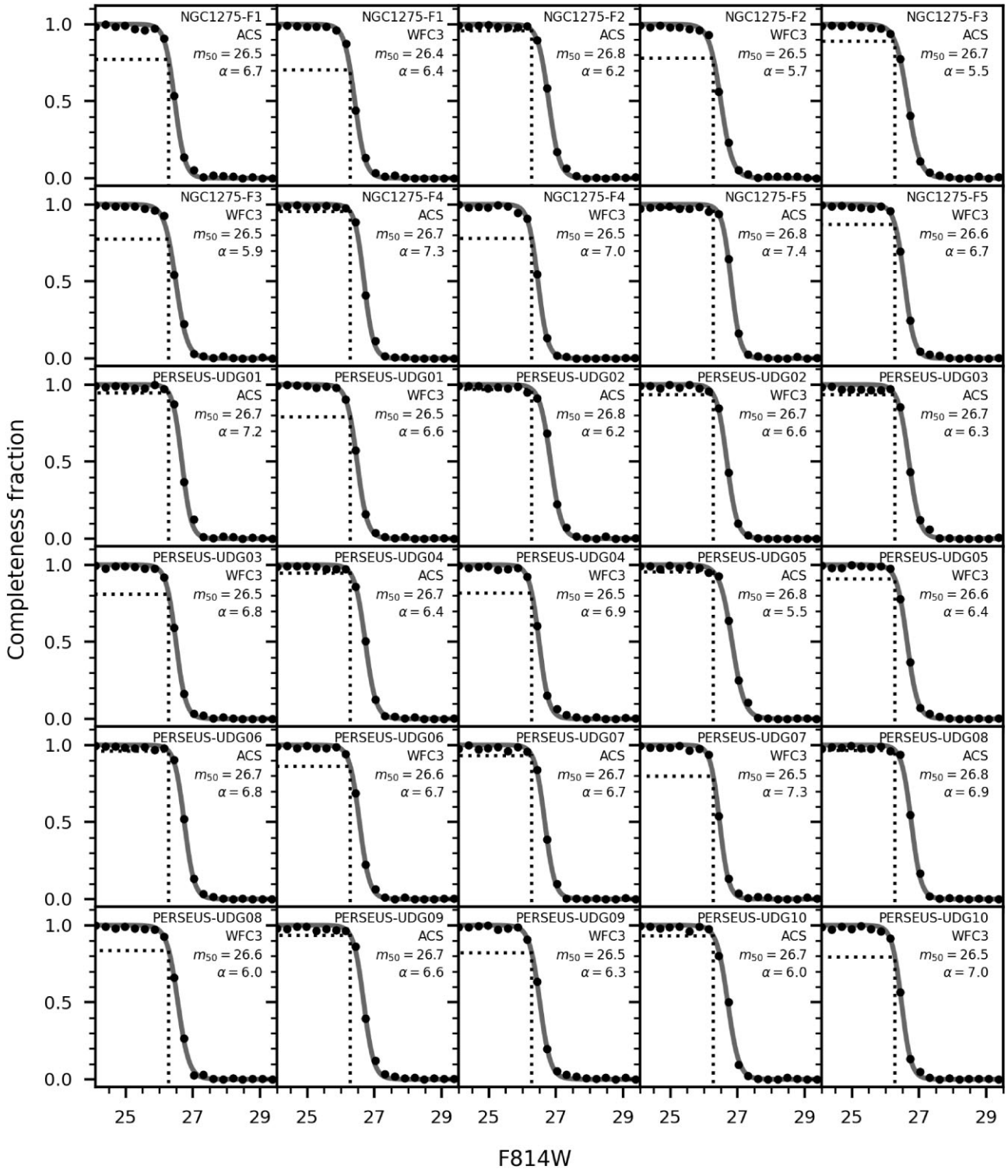

Figure A1. F814W completeness curves for all 30 fields (15 visits with parallel ACS and WFC3 pointings) as a function of input artificial star magnitude. The points are the fraction of artificial stars recovered in bins of size 0.25 mag. The solid line is the best-fitting function following equation (2). Inset text in each panel lists the visit name, camera, 50 per cent completeness limit m_{50} and α. The dotted line marks the completeness level at the predicted turnover magnitude of the GCLF ($m_{\mathrm{TO,F814W}} = 26.3$).

This paper has been typeset from a TEX/LATEX file prepared by the author.